Biophysical *Journal*
Article

Biophysical Society

Cholesterol Depletion by MβCD Enhances Cell Membrane Tension and Its Variations-Reducing Integrity

Arikta Biswas,[1] Purba Kashyap,[1] Sanchari Datta,[1] Titas Sengupta,[1] and Bidisha Sinha[1,*]
[1]Department of Biological Sciences, Indian Institute of Science Education and Research Kolkata, Mohanpur, West Bengal, India

ABSTRACT Cholesterol depletion by methyl-β-cyclodextrin (MβCD) remodels the plasma membrane's mechanics in cells and its interactions with the underlying cytoskeleton, whereas in red blood cells, it is also known to cause lysis. Currently it's unclear if MβCD alters membrane tension or only enhances membrane-cytoskeleton interactions—and how this relates to cell lysis. We map membrane height fluctuations in single cells and observe that MβCD reduces temporal fluctuations robustly but flattens spatial membrane undulations only slightly. Utilizing models explicitly incorporating membrane confinement besides other viscoelastic factors, we estimate membrane mechanical parameters from the fluctuations' frequency spectrum. This helps us conclude that MβCD enhances membrane tension and does so even on ATP-depleted cell membranes where this occurs despite reduction in confinement. Additionally, on cholesterol depletion, cell membranes display higher intracellular heterogeneity in the amplitude of spatial undulations and membrane tension. MβCD also has a strong impact on the cell membrane's tenacity to mechanical stress, making cells strongly prone to rupture on hypo-osmotic shock with larger rupture diameters—an effect not hindered by actomyosin perturbations. Our study thus demonstrates that cholesterol depletion increases membrane tension and its variability, making cells prone to rupture independent of the cytoskeletal state of the cell.

INTRODUCTION

Cholesterol is one of the key components of cell membranes in mammalian cells (1,2) and is implicated in several cellular functions (3–8), including the formation of membrane structures essential for cellular integrity (9–12) during stress. Although cholesterol-sensitive structures like caveolae are important (9,13,14) for tension regulation during stress in some cell types, red blood cells (RBCs), devoid of caveolae, are known to rupture solely by cholesterol depletion (15). Cholesterol is believed to be a critical factor in cell membrane tension regulation (16) because it can impact the different physical mechanisms used for membrane homeostasis (17). In model membranes, cholesterol content not only alters the basic mechanical parameters like bending rigidity (18) and elastic modulus (19), it also changes the resistance to rupturing on stress (increasing the line tension (19,20)). We therefore ask how cholesterol depletion in cells affects the membrane topology and dynamics, membrane tension and interaction with cytoskeleton, and cellular integrity on stress.

Cholesterol is depleted by methyl-β-cyclodextrin (MβCD), which encapsulates hydrophobic entities of the plasma membrane in its inner hydrophobic cavity (21) and extracts cholesterol from the outer leaflet continuously (22). Cholesterol extraction by MβCD is widely used in cell biology research (22), and cyclodextrins are proposed drug carriers in anticancer therapies (23). Although cholesterol enrichment in artificial lipid bilayers shows decreased membrane fluidity (19) and membrane viscosity, enrichment on endothelial cell membranes has been reported to cause a decrease in membrane surface viscosity (7) and a weakening of the membrane-cytoskeleton adhesion (3,7,24,25). Studies report cholesterol depletion suppressing lateral diffusion of lipid analogs in the cell membranes (7) while increasing membrane-cytoskeleton attachments and stiffening the cell membrane in aortic endothelial cells (3,7). These differences may arise because of the different membrane compositions between bilayers and cells or because of the effect of the underlying cytoskeleton in live cells (26). Therefore, the

Submitted July 9, 2018, and accepted for publication March 14, 2019.

*Correspondence: bidisha.sinha@iiserkol.ac.in

Purba Kashyap's present address is Division of Biochemistry, Free University Berlin, Berlin, Germany.

Sanchari Datta's present address is Department of Cell Biology, UT Southwestern Medical Center, Dallas, Texas.

Titas Sengupta's present address is Yale School of Medicine, New Haven, Connecticut.

Editor: Dimitrios Stamou.

https://doi.org/10.1016/j.bpj.2019.03.016

current understanding of the effect of cholesterol on membrane mechanics in cells lacks a clear understanding—unlike in model membrane systems (19)—and needs experimental measurements that can probe the altered membrane tension as well as the altered attachment to cytoskeleton.

Recent studies lay down models (27) that can be used to explain fluctuation spectra that have a contribution of membrane's attachment to the cytoskeleton via linkers. This is consistent with the incorporation of membrane confinement (net effect of membrane-cytoskeleton attachments and membrane-substrate hydrodynamic interactions (28)) and helps measure the membrane's tension as well as its degree of membrane confinement in systems ranging from RBCs (29) to nucleated cells (27) and neurons (30). Despite this distinction, it may be noted that fluctuations spectroscopy yields the "membrane mechanical tension" as opposed to "intrinsic bilayer tension" (31). In this study, we have used interference reflection microscopy (IRM) (32–37) to map spatiotemporal membrane fluctuations. Membrane topology (37), spatial (correlation lengths) and temporal (correlation timescales, PSD, SD of fluctuations, and spatial heterogeneity of fluctuations) parameters of fluctuations (38), and membrane dynamics are captured and calculated from images of live untreated and MβCD-treated cells. To measure membrane tension, we use models that include membrane confinement besides other viscoelastic parameters—so that the effect of membrane-cytoskeleton adhesion energy doesn't directly get incorporated in the estimated membrane tension.

Besides altering the membrane tension, cholesterol content can change the lysis tension in model membranes (39). Does this also happen in cells? The ability to resist lysis is an important property of lipid membranes in cells (40). However, stresses generated or received by organs (flow of fluid on endothelial cells, flow of RBCs, continuous stretching and relaxation of muscles, etc.) can generate physiological ruptures (41). Cells rupture when a critical tension (lysis tension) is overcome, and the area strain on lipids crosses a threshold. Theoretical studies indicate that whereas pores of sizes below a critical radius rapidly reseal by line tension, larger pores make the membrane unstable (40,42). Thus, pores that are responsible for rupturing reach a critical radius when the critical tension is attained. Membrane ruptures have so far been studied either by electroporation (40,42) or photoinduced membrane ablation (43). Unlike these techniques that apply local stresses at specific locations on membranes, physiological stresses are global stresses. The impact of cholesterol depletion on cell membrane integrity is also addressed in this study—by applying global mechanical stress (hypo-osmotic shock) on cells. Measurements of the percentage of ruptured cells and kinetics of the decay of trapped fluorophores in HeLa cells and RBCs are analyzed—the former representing cells with endomembrane and caveolae, whereas the latter lacks both. Comparing our results with known models of the lysis tension, line tension, and rupture/pore diameter (40,42,44), we draw inferences about the possible effects of cholesterol depletion on line and lysis tension.

METHODS

Cell culture

Mammalian cells (HeLa, CHO-K1, and C2C12) are grown in Dulbecco's modified essential medium (DMEM) (Gibco, Life Technologies), supplemented with 10% fetal bovine serum (FBS) (Gibco), and 1% Anti-Anti (Gibco) at 37°C, 95% humidity, and 5% CO_2.

Preparation of RBCs

Human RBCs are prepared freshly before each experiment by pricking the finger of a healthy human donor (according to the Institute Ethics Committee approval). Blood (<100 μL collected) is centrifuged at 1000 $\times$ g at 4°C for 10 min (45). The supernatant (consisting of plasma, white blood cells, and platelets) is carefully removed. The pellet containing the RBCs is resuspended in 1$\times$ Hank's balance salt solution ((+Calcium Chloride, +Magnesium Chloride) Gibco). 150 μL of this resuspended solution is plated on fibronectin (25 μg/mL)-coated coverslips and incubated at 37°C for 3 h.

Filipin III staining

Cells are fixed with 4% paraformaldehyde (Sigma) for 15 min and incubated with 0.05 mg/mL Filipin III (Santa Cruz Biotechnology) in the dark for 2 h.

Pharmacological treatments

Cells are incubated with 10 mM MβCD (Sigma) in FBS-free DMEM for 50 min (10) to deplete cholesterol. 10 mM sodium azide (Sigma) and 10 mM 2-deoxy D-glucose (Sigma) are added in M1 Imaging medium (150 mM NaCl (Sigma), 1 mM $MgCl_2$ (Merck), and 20 mM HEPES (Sigma)) for 60 min (46) for ATP depletion. Cells are incubated with 5 μM cytochalasin D (Cyto D))Sigma) for 60 min to inhibit the polymerization of actin filaments (47). To check the effect of MβCD on ATP-depleted cells, cells atop an onstage microscope incubator in M1 medium are incubated with ATP-depleting reagents for 30 min and then with MβCD for 30 min (without medium replacement). This treatment is termed as ATP dep.+MβCD. To check the role of actomyosin on membrane ruptures, cells in FBS-free DMEM are treated with Cyto D for 60 min and then with MβCD for 50 min without replacing the medium (Cyto D + MβCD). The reverse order of treatments is denoted as MβCD + Cyto D in the study. All the incubations are done at 37°C.

IRM imaging

For IRM imaging (32–37), cells are imaged in an onstage 37°C incubator (Tokai Hit, Japan) atop a Nikon Eclipse Ti-E motorized inverted microscope (Nikon, Japan) equipped with adjustable field and aperture diaphragms, 60$\times$ Plan Apo (numerical aperture (NA) 1.22, water immersion), a 1.5$\times$ external magnification, and an electron-multiplying charge-coupled device (Evolve 512 Delta; Photometrics). For IRM, an additional 100 W mercury arc lamp, an interference filter (546 $\pm$ 12 nm), and a 50-50 beam splitter is used (38), and images are recorded at electron-multiplying gain 30 and exposure time 50 ms for 102 s at 19.91 frames/s (2048 frames).

Fluorescence imaging

Filipin III-stained cells are imaged using the 4′,6-diamidino-2-phenylindole filter on the microscope, objective, and camera used previously. Images are captured at 300 ms.

Calculation of spatiotemporal fluctuations parameters

MATLAB (The MathWorks, Natick, MA) is used to calculate the relative height of the basal plasma membrane of the cell from the intensities in each pixel of an IRM image by comparing with IRM images of beads (60-μm diameter polystyrene beads; Bangs Laboratories) imaged on the same day (38). In brief, we use a bead-based calibration system to find the intensity to height conversion factor, and then we identify pixels in images of cells in which this calibration holds true.

For calibration, beads stuck on glass are imaged with different exposure times to generate images of interference fringes with varying contrast. Radial intensity profiles yield the conversion factor from intensity difference (ΔI) to height difference (Δh) for the region falling between the first minima and the first maxima. Because this is the first branch of the periodic intensity profile, pixels with intensities falling in this regime are called first branch regions (FBRs). Next, cells are imaged at a preset exposure time and electron-multiplying gain. Minimal, maximal, and background intensities from the cell images are extracted. Bead images with S (maxima + minima) matching the cell's background and having similar D (maxima − minima) are identified from the already collated list, and the corresponding conversion factor is used for intensity to height conversion.

This way of intensity-height conversion works because the difference in "reflectivity" between the bead and the cell is taken care of by imaging beads at different exposure times (38). It must be noted that the refractive index of the external medium is very important for the correct calibration (38), and hence, beads and cells are always imaged in the same external medium. It is also known that in cases of multiple reflections, the ΔI to Δh conversion will remain similar (38).

Parameters of temporal fluctuations and spatial undulations are measured only for those pixels that qualify as FBRs in cells. Such pixels are identified by first noting pixels with minimal and maximal intensities in the cell. We invoke the fact that those pixels that are spatially contiguous with "minima" pixels without having any "maxima" pixels in between must be those in which the membrane must be at a height less than that at which the first maxima occurs (38). These pixels are termed FBRs in the cell. The height of the membrane in these regions are $<\sim$100 nm and lie in the first branch of the interference pattern. We further limit our analysis to areas of 12×12 pixels (also referred to as 144 pixels herein), 2.16×2.16 μm^2 for consistency (38).

The parameters of spatial undulations (Table S1) include SD_{space} and correlation length, λ. SD_{space} is calculated from the SD of relative heights across 144 pixels within an FBR and averaged over 20 frames. λ is calculated from three-term exponential fits of spatial autocorrelation functions (ACFs) of heights across 35×10 pixels, averaged over 200 frames. The parameters of temporal fluctuations comprise of mean relative height, SD_{time}, $\overline{\sigma(0.01\ Hz,\ 0.1\ Hz)}$, $\overline{\sigma(0.1\ Hz,\ 1\ Hz)}$, and correlation time, τ. The mean and SD of relative heights calculated in each pixel over 2048 frames and averaged across 144 pixels are termed as mean relative height and SD_{time}, respectively. To see the frequency dependence of the amplitude of fluctuations, power spectra are plotted. $\bar{\sigma}$ is calculated as the root of the total area under the power-spectral density (PSD) curve between the mentioned frequencies. The slope of log(PSD) versus log(frequency) at frequency band −0.04 to 0.4 Hz is computed to understand the effect of damping in our systems and termed as exponent. We also plot f (ratio of background subtracted PSD of treated to that of control) with frequency to check for frequency-dependent altered fluctuations. τ is calculated from three-term exponential fits of temporal ACFs of heights across 2048 frames, averaged over 2×2 pixels.

Mechanical parameters' (Table S2) active temperature (A), effective cytoplasmic viscosity (η_{eff}), confinement (γ), and membrane tension (σ) are computed from fitting the PSDs of FBRs to $PSD(f) = 4\eta_{eff}Ak_BT/\pi \int_{q_{min}}^{q_{max}} dq/((4\eta_{eff}(2\pi f))^2 + [\kappa q^3 + \sigma q + (\gamma/q)]^2)$ (27,38,48). We have fixed the value of bending rigidity (κ) at 15 k_BT (49). Maps of all mechanical parameters are generated by extracting those from fitting PSDs of every pixel to the theoretical model.

Intra-FBR heterogeneity (SD (SD_{time})) is calculated from SD of SD_{time} of pixels over 2048 frames and across 144 pixels. To compute long-range variability within cells, the SD_{time} of all 144 pixels in an FBR is statistically compared to those in every possible FBR in pairs, and the p value from a one-way analysis of variance is calculated. The number of FBR pairs having dissimilar SD ($p < 0.001$) is found out, and the ratio of this value to the total number of possible FBR pairs is termed as dissimilar FBR pairs. We use this as a measure of intracellular long-range heterogeneity. Intracellular heterogeneity is also calculated by calculating the SD of all values of SD_{time}, SD_{space}, and σ across all FBRs in each cell (Table S1).

Hypo-osmotic shock-induced rupture experiments

Cells are incubated with 2.5 μM Calcein AM (Invitrogen) at 37°C for 30 min, washed well before, and fresh medium (with/without drugs) added for further experiments. Images are acquired with at 10× Plan Apo objective (NA 0.45) with a 1.5× external magnification with 100 ms exposures and at 0.5 frames/s for 5 min. For hypo-osmotic shock, DMEM diluted in deionized water (1/20× for 95% shock) is used. For RBCs, the hypo-osmotic shock is 67%, and the acquisition rate is 2 frames/s. To calculate rupture propensity, cells are scanned 15–30 min after the hypo-osmotic shock. Multiple fields are captured in the differential interference contrast (DIC) and epifluorescence. From DIC, the total number of cells (N_t) present in each field is counted, and from epifluorescence, the total number of fluorescent (hence, not ruptured) cells (N_{nr}) in the same fields is counted. Rupture propensity (R_P) in that field is calculated as: $R_p = (N_t - N_{nr})/N_t$.

Estimation of rupture diameter

Calcein AM fluoresces on permeating live cells (43,50). The trapped fluorescent Calcein moves out of the cell only if it ruptures and results in a sudden drop in its fluorescence. A model based on simple diffusion (assuming Calcein moves out of the cell by diffusion through the rupture site) is used to estimate rupture diameter (43). The time series of normalized mean intensity (normalized with first frame) of a region inside each cell is plotted, and the ones showing ruptures fitted with $f(t) = Ae^{-(t/\tau_r)} + Ce^{-(t/\tau_p)}$, where τ_r is used as the timescale, whereas τ_p arises from photobleaching, if any. Assuming the radius (R) of a typical HeLa cell is 20 μm (and $V = 4\pi R^3/3$ and V = 100 μm^3 for RBCs), l is 7 nm, and D is 330 $\mu m^2/s$, rupture diameter, r_D is calculated from: $r_D = 2\sqrt{Vl/\pi\tau_r D}$.

Statistical analysis

Calibration of IRM with beads and control experiment with cells without any treatment are performed with each IRM experiment. At least 10 cells are imaged for each condition and ~20–40 FBRs analyzed for each cell. In most cases, analysis is collated over at least three sets of experiments performed on different days. Mann-Whitney U test is performed to determine the statistical significance ($*p < 0.05$, $**p < 0.001$).

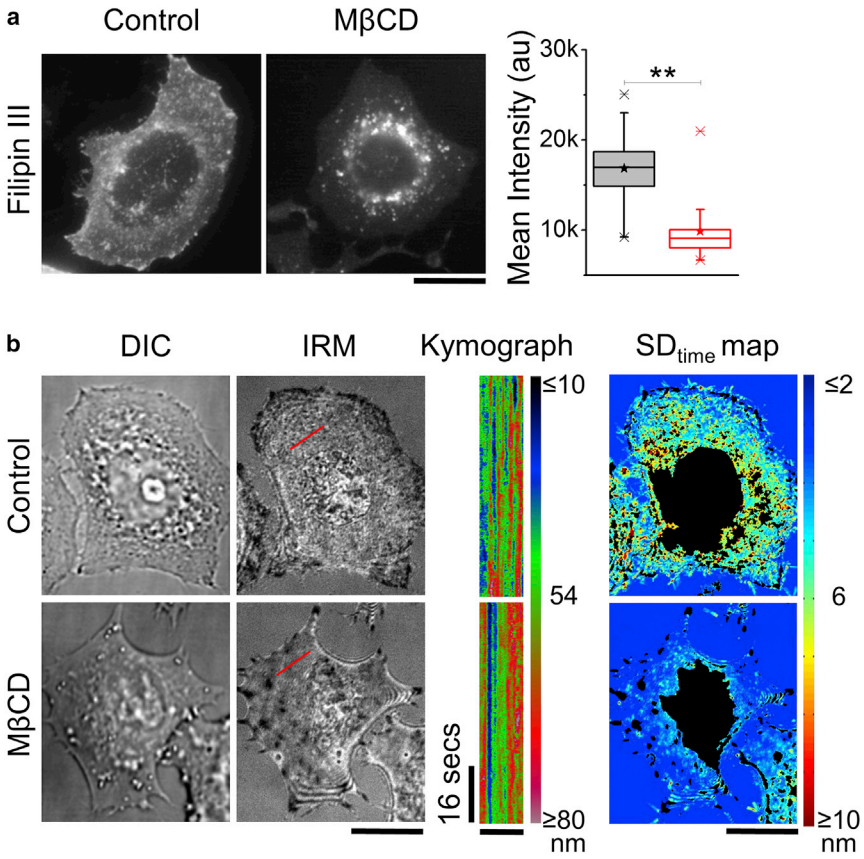

FIGURE 1 Effect of MβCD-mediated cholesterol depletion on membrane topology. (*a*) Left: representative fluorescence images of Filipin III-stained control and MβCD-treated HeLa cells are shown. Right: shown is a box plot of mean intensity of Filipin III in cells in mentioned conditions (N = 30 cells each). Center lines of boxes show the medians; stars show the means; box limits indicate the 25th and 75th percentiles; and whiskers extend 1.5 times the interquartile range from the 25th to 75th percentiles. $^{**}p < 0.001$, Mann-Whitney U test. (*b*) Shown are representative DIC (first), IRM (second) images, kymographs of regions overlaid on the images in red (third, scale bars in y, 16 s, scale bars in x, 5 μm) and corresponding SD_{time} maps of control versus MβCD-treated cells (non-FBRs blacked out). Scale bars, 10 μm. See Table S3 for statistics. To see this figure in color, go online.

RESULTS

MβCD treatment decreases temporal fluctuations and flattens out spatial undulations

HeLa cells are depleted of cholesterol by MβCD and stained with Filipin III to check for cholesterol depletion (Fig. 1 *a*, left). As seen in earlier reports (51), images show Filipin III staining at the plasma membrane in control cells, which is lost on MβCD treatment, thereby increasing the contrast of the intracellular vesicles. A quantification of mean Filipin III fluorescence at the membrane shows a ∼40% (N = 30 cells) decrease on cholesterol depletion (Fig. 1 *a*, right). In Fig. 1 *b* and Video S1, IRM imaging reveals the altered membrane topology and slower z-movements (seen as intensity variations) of the basal plasma membrane on MβCD treatment. The reduced intensity variations are better visualized by the color-coded kymographs (Fig. 1 *b*). For quantification, we convert intensity in the images to relative heights (38) as described in the methods and calculate different spatiotemporal parameters (Table S1). The most robustly affected parameter of the height fluctuations is the root mean-squared amplitude of the time variation of membrane height at any pixels (SD_{time}). The reduction of SD_{time} on MβCD treatment is evident from SD_{time} maps (Figs. 1 *b* and S1 *a*), from single cell statistics in which the average SD_{time} for each cell (Fig. S1 *b*) is plotted and from single FBR statistics obtained from ∼1500 FBRs across ∼70 cells per condition (Fig. S1 *c*). The relative height (reference zero same for both control and MβCD) is seen to increase on cholesterol depletion.

In Fig. 2 *a*, we plot the PSD for the two conditions. PSD is lowered by MβCD—the effect being more prominent at lower frequencies (∼0.01–0.1 Hz) (Fig. 2 *a*, inset). Calculated amplitudes ($\overline{\sigma}$) at both frequency bands—0.01–0.1 Hz and 0.1–1 Hz—show a significant reduction on cholesterol depletion (Fig. 2 *b*). The PSD's power-law dependence on frequency, captured by the exponent, increases (from −4/3 to −1) on MβCD treatment (Figs. 2 *b* and S1 *c*), implying increased confinement (52,53). All these temporal parameters are significantly affected and captured both in single FBR (Fig. S1 *c*) as well as single cell statistics (Figs. 2, *a* and *b* and S1 *b*).

MβCD leads to a small decrease in the root mean-square amplitude obtained from snapshots of local height profiles (2.16 × 2.16 μm) (SD_{space}) for the same sets of cells (Fig. S1 *c*). In parallel, a slight flattening of the spatial ACF (Fig. S1 *d*) is also obtained from snapshots of local height profiles (6.3 × 1.8 μm), leading to a slight (8%: from 0.49 ± 0.27 μm to 0.53 ± 0.28 μm) increase in the spatial correlation length scale (λ) (Fig. 2 *c*). However, in all these spatial parameters, the difference is significant

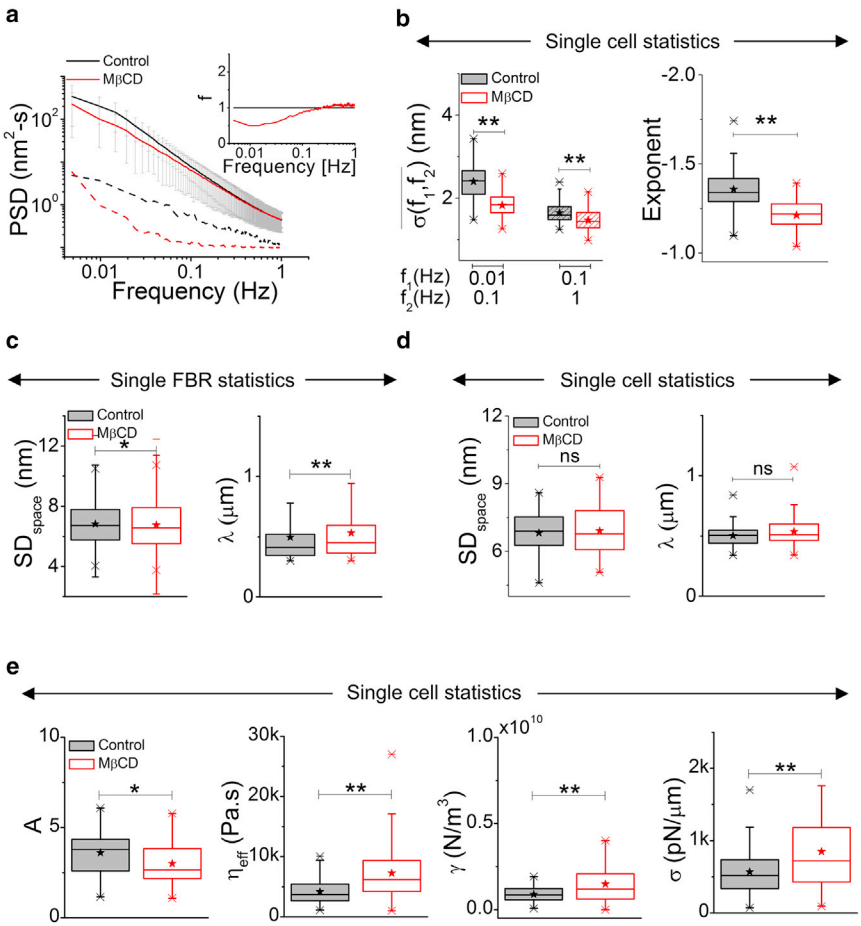

FIGURE 2 Cholesterol depletion by MβCD reduces temporal fluctuations and enhances membrane tension. (*a*) Shown are averaged PSDs of FBRs in MβCD-treated cells and their controls (*solid lines*) with their backgrounds (*dashed lines*); inset shows f (ratio of background subtracted PSDs). (*b*) Left: Shown are box plots of $\overline{\sigma(f_1,f_2)}$ in two different frequency regimes. Right: exponent in the two conditions is shown. N = 70 cells each. (*c*) Left: single FBR statistics of SD_{space} in control and cholesterol-depleted cells. $n_{control}$ = 1683 FBRs, $n_{M\beta CD}$ = 1471 FBRs, and N = 70 cell each. Right: correlation lengths are shown. (*d*) Single cell statistics of SD_{space} (*left*) and correlation lengths (*right*) in the two conditions are shown. N = 70 cell each. (*e*) Shown are box plots of mechanical parameters A, η_{eff}, γ, and σ in control and MβCD-treated cells. N = 70 cell each. $^*p < 0.05$, $^{**}p < 0.001$, Mann-Whitney U test. See Fig. S1 and Tables S1–S3 for statistics. To see this figure in color, go online.

only in single FBR statistics but not in single cell statistics, possibly because of the spatial intracellular nonuniformity.

Cholesterol depletion by MβCD increases membrane tension

We next compute membrane mechanical properties by fitting the PSDs with a theoretical model (38) to further characterize the effect of cholesterol depletion. The model is based on Helfrich Hamiltonian (48), which predicts the PSD (31,54) of a membrane of defined tension (σ), bending rigidity (κ) in a viscous surrounding (of effective viscosity, η_{eff}). We include adaptations as used in past theoretical (27,55) and experimental studies (29,30,56) that also consider the effect of γ confinement (27,29,55). Further, we use the notion of "active temperature" to capture the effect of random active forces on the membrane. Herein, temperature is increased by a factor of "A" (52,57). Note that these models have been used in both liposomes (54) as well as blebs on cells (56) and cells (29,30,38,58).

On fitting with κ fixed at 15 k_BT (49), although varying the other four, single cell statistics demonstrates that cholesterol depletion leads to a significant decrease in A and a significant increase in η_{eff}, γ, and σ (Fig. 2 *e*; Table S3). We note that the change in η_{eff} and σ persists in single FBR statistics; however, change in γ is found to be insignificant (Fig. S1 *e*; Table S4).

The values obtained for the four unknown mechanical parameters for control cells are close to numbers found in past reports. Specifically, A ranges ~1–10 (57), η_{eff} ranges ~1–10^6 Pa s (59,60), γ ranges ~0–1 × 10^{10} N/m^3 (27,52), and σ ranges ~10–450 pN/μm (56,61). Confinement, thus accounted, may originate from the membrane's interactions with the cytoskeleton (27) or substrate (53). A high η_{eff} may originate from effective viscosity of the underlying actomyosin gel or from molecular pins impeding membrane flow (60,62–65). This range of numbers has been both predicted for actomyosin gels (60) as well as experimentally observed (59).

We show that fits to the PSD are sensitive to each parameter for typical fits (Fig. S2 *a*). We also plot expected PSDs on varying each of the parameters around the value used in fits (ranges chosen from known values (Table S2)) displaying the frequency range affected by each parameter (Fig. S2 *b*). A alters the complete PSD as a multiplicative factor, η_{eff} changes the shape of the PSD, hence altering the lower to higher frequency ratio, γ alters only the lower frequency regime, and σ affects both lower and higher frequencies.

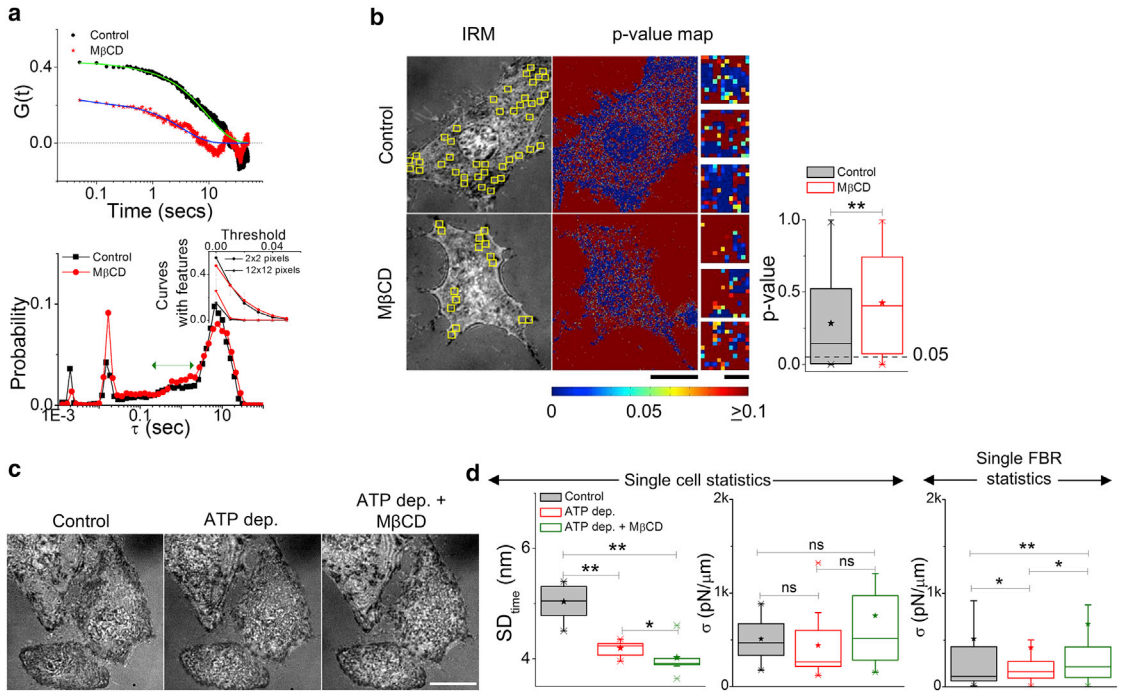

FIGURE 3 MβCD treatment does not abrogate signatures of activity. (*a*) Top: shown are the typical temporal ACFs of single 2 × 2 pixels FBRs in control and MβCD-treated cells, along with their fits to a three-term exponential function. Bottom: shown is the weighted distribution of correlation timescales (τ) obtained from the temporal ACFs. The green arrow marks the timescales for active fluctuations. Inset shows a plot of the fraction of curves with features versus threshold used to detect the features ($n_{control}$ = 2890 fits, $n_{M\beta CD}$ = 3071 fits, and N = 21 cells each). (*b*) Shown are FBRs overlaid in yellow on IRM images and their corresponding whole cell (Scale bars, 10 μm) and FBR (Scale bars, 1 μm) *p* value maps (Kolmogorov-Smirnov hypothesis testing). Right: Shown is the *p* value for FBRs in control versus cholesterol-depleted cells. $n_{control}$ = 53,568 pixels, and $n_{M\beta CD}$ = 42,480 pixels. (*c*) Shown are the representative IRM images of control, ATP dep., and ATP dep. + MβCD cells. Scale bars, 10 μm. (*d*) Box plot for SD_{time} (*left*) and σ (*middle*) for these conditions. N = 10 cells. Right: Shown are single FBR statistics of σ in the three conditions. nc_{ontrol} = 305 FBRs, $n_{ATPdep.}$ = 207 FBRs, $n_{ATPdep.+M\beta CD}$ = 229 FBRs, and N = 10 cells each. *$p < 0.05$, **$p < 0.001$, ns $p > 0.05$, Mann-Whitney U test. See Fig. S3 and Tables S1–S3 for statistics. To see this figure in color, go online.

To understand which parameter drives the effect of MβCD on the PSD, we simulate PSDs by using fit parameters (control set) and by switching one parameter at a time of the control set to that for MβCD-treated cells. We then calculate SD from these simulations, plot the expected change in SD ($SD_{control\ set}/SD_{simulated}$), and see that changes in σ results in the most significant reduction of SD (Fig. S2 *c*). We also check the values and patterns of all mechanical parameters by keeping one or more parameters constant. It is seen that fixing confinement or tension decreases fitting efficiency stronger than fixing other parameters (Fig. S2 *d*). It needs to be noted that shear modulus arising because of the cytoskeleton's connection with the membrane, which past studies have included in their model (29), when incorporated in our fitting model resulted in values contributing to the PSD ~100 times lesser than σ and hence not considered in the final fits (Fig. S2 *e*). These set of checks underscore the robustness of the effect of MβCD on membrane tension (Fig. S2 *e*).

Active signatures retained on MβCD treatment

We next ask how cholesterol depletion affects the contribution of activity-driven processes to the observed fluctuations. Temporal ACFs and the distribution of correlation timescales (τ) (Fig. 3 *a*) and Gaussian-ness of fluctuations are calculated toward this (Fig. 3 *b*). ACFs reflect reduced correlation strengths on MβCD treatment (Fig. 3 *a*, *top*). The distribution of correlation timescales, however, retains the peak in the 0.2–2 s range among other peaks (Fig. 3 *a*, *bottom*). This range is usually under-represented when ATP-dependent metabolic activity is hampered by ATP depletion or when fluctuations of plasma membrane spheres are evaluated (38). The other signature of active fluctuations is the presence of "bumps" (local peak-like features) in ACFs (proposed to be caused by correlated kicks on the membrane), which are known to be reduced in ATP-depleted cells (29,38) and in plasma membrane spheres (38). Herein, we find that similar proportions of ACFs have "bumps" (Fig. 3 *a*, *bottom inset*) and there is a drop in this fraction (like that of control) on increasing the region of averaging from 2 × 2 pixels (0.36 × 0.36 μm) to 12 × 12 pixels (2.16 × 2.16 μm). Thus, despite the decrease in correlation strength, the fraction of curves with bumps are not affected by cholesterol depletion. Is the level of "Gaussian-ness" of fluctuations in these cells also retained? We map the *p* values of Kolmogorov-Smirnov hypothesis testing to

quantify the similarity of the temporal fluctuations at each pixel with Gaussian distributions—in which higher p values indicate greater similarity to Gaussian fluctuations (Fig. 3 *b*, *left*). We find that the p values increase significantly on MβCD treatment (Fig. 3 *b*, *right*). Such an increase may either result from the loss of ATP-dependent fluctuations (38,66) or may be a result of a reduction in the strength of fluctuations. On analyzing data for mitotic cells, in which fluctuation strength reduces with respect to interphase cells, we find an increase in Gaussian-ness. These cells are expected to retain ATP-dependent activities as also corroborated by the existence of correlation timescales at 0.2–2 s. Herein, the level of Gaussian-ness is thus determined more by the strength of the fluctuations than by the relative contribution of ATP-dependent fluctuations—consistent with studies describing nonequilibrium fluctuations retaining their Gaussian nature (67). On MβCD treatment, although the relative contribution of ATP-dependent fluctuations persists, fluctuations reduce and are less autocorrelated. Does MβCD treatment, therefore, physically affect the membrane irrespective of the cell's metabolic state?

MβCD treatment also affects ATP-depleted cells

We use ATP-depleted cells to test the effect of MβCD and once again find reduced temporal fluctuations (Figs. 3, *c* and *d* and S3, *a* and *b*)—significant both in single cell and single FBR (>250 FBRs in each condition, Fig. S3 *c*) statistics. Though we do not see enhanced tension in the single cell statistics (N = 10), single FBR statistics show that tension is enhanced on MβCD treatment of ATP-depleted cells. We do not see a significant change in SD_{space} when MβCD is treated on ATP-depleted cells (Fig. S3 *d*). Note that although the changes in the mechanical parameters are nonsignificant in single cell statistics, we find decreased γ, decreased A, and enhanced η_{eff} in single FBR statistics (Fig. S3 *e*). Hence, MβCD reduces temporal fluctuations robustly, but the effect of increasing tension is less pronounced and, although evident at subcellular length scales, becomes less significant on being averaged.

MβCD enhances intracellular mechanical heterogeneity

We next seek to understand the effect of cholesterol depletion on the spatial heterogeneity and characterize both short- (inside an FBR, <2.16 μm) and long-range heterogeneity (distances ranging from 2.16 to 54 μm). To compute short-range or local heterogeneity, we calculate the intra-FBR variation in amplitude of temporal fluctuations as the SD (SD_{time}) and find a reduction in this quantity (even after the averaging of each cell and using single cell statistics) on MβCD treatment (Figs. 4 *a* and S1 *c*). Long-range heterogeneity is first quantified by comparing all possible pairs of FBRs in cells and obtaining the p values (of SD_{times}) to segregate similar ($p > 0.001$) and dissimilar ($p < 0.001$) FBR pairs. The percentage of dissimilar FBR pairs increases on cholesterol depletion (Fig. 4, *b* and *c*). Next, we quantify the intracellular variability of SD_{time}, SD_{space}, and σ by calculating the SD of these parameters from measurements done at every FBR for any cell. Such single FBR statistics show that intracellular variation of SD_{time} is not affected by cholesterol depletion but that of SD_{space} and σ are significantly enhanced (Fig. 4 *d*). This is in line with weaker statistical changes for both SD_{space} and σ on cholesterol depletion when evaluated by single cell statistics than single FBR statistics. On mapping mechanical parameters, we find a visual proof of enhanced intracellular heterogeneity in σ on MβCD treatment (Figs. 4 *e* and S4).

We further investigate the generality of this effect by testing the impact of MβCD on another epithelial cell line CHO and a mouse myoblast cell line C2C12. CHO, unlike HeLa, has a robust CLIC/GEEC (CG) endocytosis pathway (68), making the possible active mechanisms for its tension regulation different from that of HeLa.

Multiple cell lines display enhanced tension on cholesterol depletion

In Fig. S5 *a*, we show parameters pertaining to fluctuations measured in CHO and C2C12 on MβCD-mediated cholesterol depletion. We see that temporal fluctuations are always reduced after MβCD treatment in both CHO and C2C12 like in HeLa (Fig. S5, *b–d*). In CHO, we report a decrease in intra-FBR variations SD (SD_{time}) (Fig. S6 *a*), whereas the changes in the spatial parameters of undulations or long-range heterogeneity are not seen to significantly alter upon cholesterol depletion (Fig. S6 *b*). It is noteworthy that MβCD leads to an increase in σ (single cell and single FBR statistics) and η_{eff} (single FBR statistics) (Fig. S6, *c* and *d*) as in HeLa. C2C12 cells, however, do not show a significant change in the short-range heterogeneity in cholesterol-depleted C2C12 cells or tension (Fig. S6, *a* and *d*)—however, they do show an enhanced correlation length scale (Fig. S5 *d*) and η_{eff} (Fig. S6 *d*).

Although γ values increased on MβCD treatment in single cell statistics in HeLa cells, we remind that no significant change was found in single FBR statistics. Also, ATP-depleted cells showed a reduction in γ on MβCD treatment (based on single FBR statistics). In CHO and C2C12 cells, γ is either not significantly altered in single cell statistics while reduced in single FBR statistics on MβCD treatment. It must be noted that γ has both the contribution of interaction of the membrane with the cytoskeleton as well as substrate—and emerges to be less robustly affected than tension.

Therefore, the most robust effect of MβCD on membrane mechanics in single cells is to reduce temporal fluctuations, increase the membrane tension and its spatial heterogeneity, and increase η_{eff}. In the next section, we address how MβCD

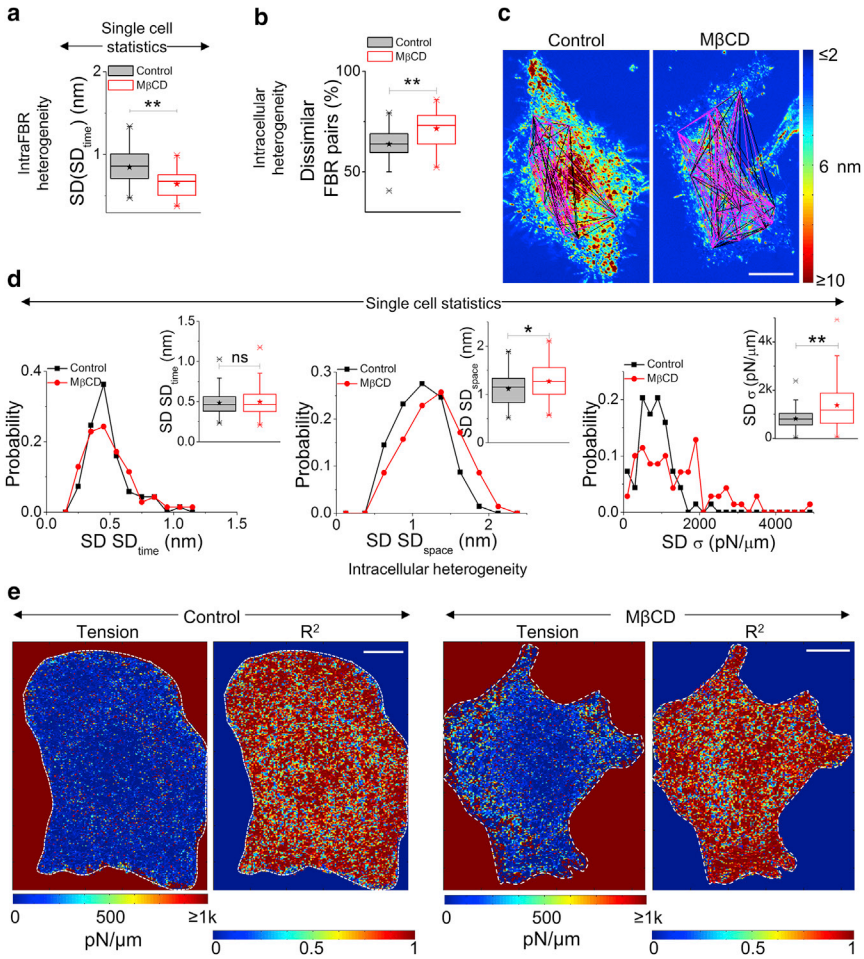

FIGURE 4 Enhanced spatial and mechanical intracellular heterogeneity on MβCD treatment. (*a*) Intra-FBR fluctuations heterogeneity measured by SD (SD_{time}) for the two conditions are shown. (*b*) Shown are intracellular long-range fluctuations heterogeneity measured by box plots of the number of dissimilar FBR pairs. Dissimilarity is evaluated by comparing SD_{time}. N = 70 cells each. (*c*) Lines in magenta and black connect FBRs that are dissimilar and similar in SD values, respectively. The lines are overlaid on the SD_{time} maps in representative control and MβCD-treated cells. Each node in the maps represents the center of an FBR. Scale bars, 10 μm. (*d*) Shown are histograms and box plots of intracellular heterogeneity of cell averaged SD_{time}, SD_{space}, and σ in the two conditions. N = 70 cells each. (*e*) Representative single pixel maps of tension (σ) and goodness of fit (R^2) for a control and MβCD-treated cell are shown. The white dashed line marks the boundary of the cell. Fitting was performed for pixels inside this boundary. Scale bars, 10 μm. $*p < 0.05$, $**p < 0.001$, ns $p > 0.05$, Mann-Whitney U test. See Figs. S1 and S4 and Tables S1–S3 for statistics. To see this figure in color, go online.

treatment alters the rupture propensity and affects the lysis tension in cells.

Cholesterol depletion increases membrane rupturing propensity and diameter on hypo-osmotic shock

We use hypo-osmotic shock to impart global mechanical stress (Videos S2 and S3) on cell membranes and assess its propensity to rupture. HeLa cells are loaded with Calcein AM and analyzed before and at least 15 min after hypo-osmotic shock. Cells with a ruptured membrane lose the internal Calcein AM and are hence identified by comparing their absence in fluorescence images to their presence in DIC images (Fig. 5 *a*). Rupture propensity is defined as the percentage of cells that undergo rupturing, and it increases the strength of the hypo-osmotic shock (Fig. 5 *a*, bottom). Rupture propensity also increases when the temperature is decreased from 37°C (0.9% ruptures) to <10°C (1.7% ruptures) or 25°C (4.2% ruptures) or increased to 42°C (2.7% ruptures). ATP depletion too increases rupture propensity but only to 5–10% (Fig. 5 *a*, bottom). We find that RBCs (Fig. S7 *a*), in general, have a much higher rupture propensity than HeLa cells. In addition to calculating rupture propensity, we also follow the Calcein AM-loaded cells (HeLa and RBCs) after hypo-osmotic shock and find that rupturing events lead to a sudden loss in internal mean intensity (Figs. 5 *b* and S7 *b*). Ratio maps (Fig. 5 *c*) between consecutive images show that the rupturing is marked by fluorescence loss from the whole cell and by a simultaneous and sudden increase of fluorescence in the surrounding medium that is often asymmetric (Figs. 5 *c* and S7 *c*). This indicates that the loss of intensity is due to a single-point rupture and is also seen in RBCs (Fig. S7 *c*, left). Fitting the temporal intensity profile (Figs. 5 *d* and S7 *c*, right) with exponential decay functions yields a time constant that is used to estimate the rupture diameter based on a simple model that assumes fluorescence loss from the lesion by pure diffusion.

MβCD treatment results in an enhanced rupture propensity and an increased rupture diameter on hypo-osmotic shock (Fig. 5 *e*). As reported earlier (15), we too see that RBCs and a small percentage of HeLa cells rupture in isotonic media when treated with MβCD (Figs. 5 *f* and S7 *e*). We also find that increasing MβCD concentration enhances rupture propensity in RBCs, whereas the rupture

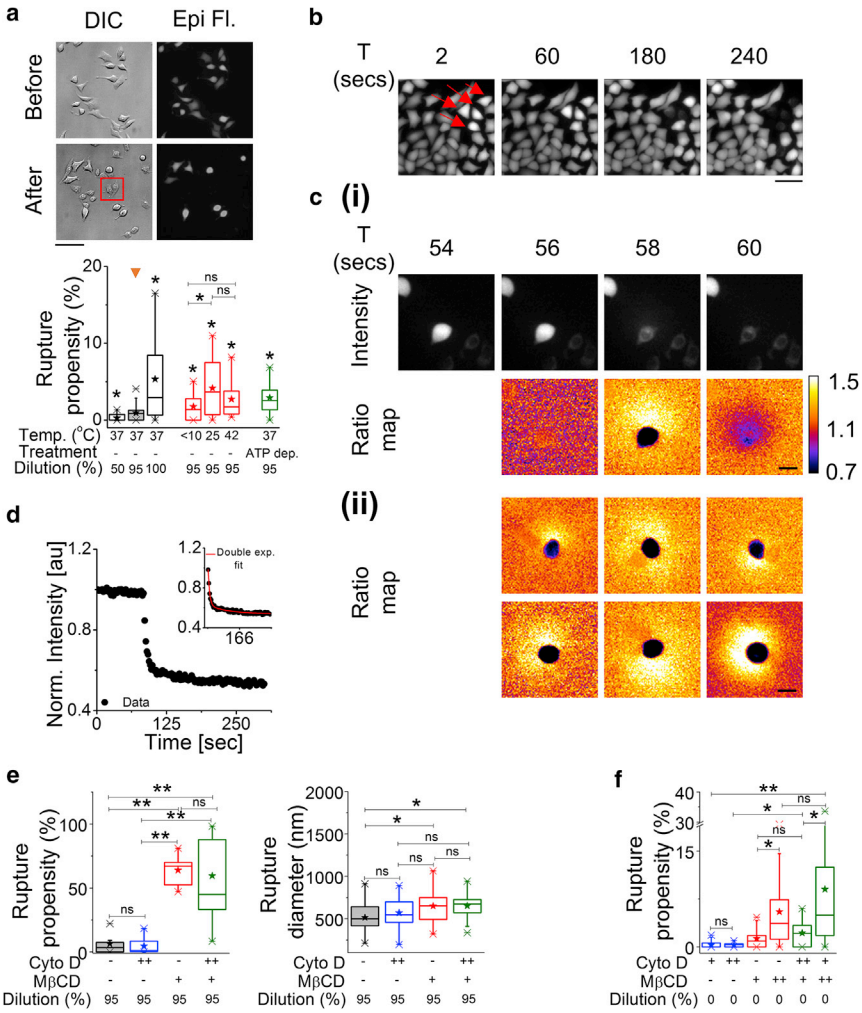

FIGURE 5 Membrane rupture induced by hypo-osmotic/iso-osmotic medium in the presence of MβCD. (*a*) Top: shown are DIC and epifluorescent images of Calcein AM-labeled HeLa cells before and after the administration of a 95% hypo-osmotic shock (Scale bars, 100 μm). Among others, the cells in the box are representatives of membrane rupture. Bottom: shown is a box plot of rupture propensity of cells due to change in hypo-osmotic stress, change in temperature, and ATP depletion (N = 3 experiments each). (*b*) Top: shown are time lapse images of Calcein AM-loaded HeLa cells undergoing rupture (arrowheads in *red*) (Scale bars, 50 μm). (*c*) (*i*) Shown is the intensity and ratio (*Intensity of frame*/*Intensity of previous* frame) map of a rupturing cell followed in time to show single point rupture. (*ii*) Shown are representative ratio maps of six different cells showing an asymmetric spread of fluorescence after rupture (Scale bars, 30 μm). (*d*) A time profile of normalized mean intensity of a ruptured cell is shown; inset shows the double exponential fit to the profile. (*e*) Shown are box plots of rupture propensity (*left*) and rupture diameter (*right*) of 95% hypo-osmotic shock administered HeLa cells under control, Cyto D (2 h post-treatment), MβCD (50 min post-treatment), and Cyto D + MβCD conditions (N = 3 experiments each). (*f*) Shown are box plots of rupture propensity of cells under Cyto D, MβCD, and dual drug treatments (N = at least three experiments each) in the absence of hypo-osmotic shock. "+" denotes 60 min treatment (for Cyto D) and 50 min (for MβCD), and "++" denotes 120 min treatment. *$p < 0.05$, **$p < 0.001$, ns $p > 0.05$, Mann-Whitney U test. See Fig. S7 and Table S3 for statistics. To see this figure in color, go online.

diameter matches that with hypo-osmotically shocked control cells (Fig. S7, *d* and *e*).

To understand the role of the cytoskeleton in the measured effect, we perform experiments in which cells are first treated with Cyto D before MβCD treatment and then a hypo-osmotic shock is administered. We find that Cyto D on its own does not alter the rupture propensity or rupture diameter on hypo-osmotic shock (Fig. 5 *e*). Similar values of rupture propensity and rupture diameter in MβCD-treated cells as well as Cyto D + MβCD cells on hypo-osmotic shock show that the effect of MβCD is not abrogated by Cyto D. This indicates that the cytoskeleton is not essential for the effect of MβCD on membrane integrity. This effect is also seen in MβCD-pretreated cells (Fig. 5 *f*) and is found to be more pronounced in RBCs (Fig. S7 *e*; Video S4).

Thus, cholesterol depletion by MβCD alters membrane mechanics by increasing the membrane tension and its heterogeneity and enhances the rupturing propensity of the membrane with or without external stress. These effects are not mediated through the enhanced membrane-cytoskeleton interactions and found to be also true in RBCs.

DISCUSSION

In this article, we use interference-based membrane fluctuation maps to quantify the effect of MβCD-mediated cholesterol depletion on cell membranes and their integrity. Our study also evaluates the intracellular variability of measured fluctuations and estimated mechanical parameters—to the best of our knowledge, unaddressed in previous studies. The most robust statistic pertains to the reduction of temporal fluctuations—a plausible consequence of the continued loss of an abundant membrane component, cholesterol, and observed in three different cell lines (HeLa, CHO, C2C12) as well as in ATP-depleted HeLa cells. Concomitantly, we observe a statistically significant increase in membrane tension in HeLa and CHO cells—although their tension regulation mechanisms may differ (68). The existence of the active regulation of membrane tension (17) raises the possibility that the observed tension increase may primarily originate from cholesterol's involvement in diverse membrane trafficking processes. However, we find that active signatures persist on cholesterol depletion,

although signal strengths reduce. Although it indicates that MβCD may not affect cells only through cholesterol's role in active processes, it doesn't establish if cholesterol depletion also directly affects the membrane and its tension. Our data on MβCD's effect on ATP-depleted cells, however, addresses this point and firmly concludes that having a metabolically active cell is not essential for the manifestation of MβCD's impact of reduced fluctuations and enhanced tension on the plasma membrane.

Alteration to the mechanical state is assessed at three length scales. The first comprises using pixel-wise information to calculate local ($2.16 \times 2.16\ \mu m^2$ regions) variation of height termed SD_{space} and that of temporal variation termed SD_{time}. Correlation lengths (0.2–10 μm) also portray length scales of this level. In the second level, averaging is performed over single FBRs, and the pool from all FBRs (from all cells) are termed as single FBR analysis. Finally, single cell statistics entails averaging data from all FBRs for cells, and pooling data (mean and SD for each cell) for all cells in each condition. The SD calculated for each cell captures the intracellular variability. Therefore, we treat regions inside cells to be possibly distinct. We comment both on how overall cell states get affected as well as how the overall median alters, and thus, we include both cell-based and FBR-based statistics for most comparisons.

Such quantifications of intracellular variability of SD_{time}, SD_{space}, and σ demonstrate that different regions in a cell may be affected to different degrees by MβCD. Although intracellular variations of SD_{time} don't significantly enhance, there are more region pairs that are statistically dissimilar on comparing their SD_{time} map. This contrasts with the effect of other treatments reported by us in the past by evaluating the number of statistically dissimilar FBR pairs, like ATP depletion, Cyto D treatment, etc. (38). Long-range intracellular heterogeneity is higher for SD_{space} as well as σ on MβCD treatment. Thus, besides changing mean values, MβCD also creates a more heterogeneous mechanical state.

Our next part shows the undesirability of mechanical conditions created by MβCD. Corresponding to its enhancement of dissimilar regions, MβCD distinctly enhances rupture propensity on hyposhock. Altering temperature, depleting ATP, or disrupting the cytoskeleton do not increase rupture propensity as strongly. We find a finite pool of cholesterol-depleted cells rupturing even without hyposhock—as also seen for RBCs. Our data suggests this to be independent of its effect on the cytoskeleton because the effect of MβCD enhancing rupturing propensity persists in cells pretreated with Cyto D. What drives membrane destabilization? Is it due to the enhanced tension, or is it due to the enhanced heterogeneity in tension?

Although membrane tension can be enhanced by ATP depletion, it marginally increases (to 5%) rupturing propensity compared to MβCD (to 50%). Because cell membranes can show slower timescales of flow of local membrane perturbations compared to model membranes (14), our data suggests that mechanical heterogeneity created by cholesterol depletion might be weak regions that cannot be equilibrated quickly and hence rupture in the advent of global cell swelling by hypo-osmotic shock. Note that ATP depletion, in fact, reduces intracellular heterogeneity of SD_{space}, something that is amplified by MβCD.

Can enhanced membrane tension alone explain the increase in rupture propensity and radius by MβCD? We undertake estimations wherein we invoke the dependence of the critical rupture size on the membrane's line to surface tension ($r = \gamma/\Sigma$) during lysis (Supporting Discussion). Estimations show that the energy (40,42) required to open the pore ($\Delta E = \pi\gamma^2/\Sigma = \pi\gamma r \sim 12\ k_BT$ (for RBCs), 200 k_BT (for HeLa), assuming a lower limit $\gamma \sim 1$ pN and using observed radii of rupture, 15 and 250 nm, for RBC and HeLa cells, respectively) is too high and contrasts the observed probability of rupture (expected ($\exp(-\Delta E/k_BT)$): 6×10^{-6}; observed: 0.092, for RBCs without hypo-osmotic shock and in the presence of MβCD). Although this already implies that the ruptures might be induced by local defects in the membrane, we believe lowered line tension (as observed in giant unilamellar vesicles (20)) and lysis tension can also lead to the observations of an enhanced propensity with similar or enhanced rupture diameter on cholesterol depletion (Supporting Discussion; Fig. S8). It is therefore not possible to conclude on the mechanism by which MβCD enhances membrane rupturing in cells.

How does this study address the issue of separating MβCD's effect on membrane-cytoskeleton attachment from its effect on membrane tension? First, we emphasize that although the cytoskeleton affects membrane fluctuations, incorporating confinement parameter in the model describing PSD, $PSD(f) = 4\eta_{eff}Ak_BT/\pi \int_{q_{min}}^{q_{max}} dq/((4\eta_{eff}(2\pi f))^2 + [\kappa q^3 + \sigma q + (\gamma/q)]^2)$, allows us to estimate both the confinement (has contribution from substrate as well as an attachment to the cytoskeleton by linker (27)) as well as the mechanical tension felt by the membrane (31). Restricting the confinement of a fixed value overestimates the effect of MβCD (Fig. S2), underscoring the importance of confinement. Having assessed both parameters, our analysis shows that the tension increase is robust and persists even when ATP-depleted cells are used for MβCD treatment. Alterations in γ by MβCD, however, is less robust, and although maps show a close correspondence between heterogenous tension and that of confinement (Figs. 4 *e* and S4), statistics show that tension is increased even when confinement is not significantly affected (Fig. S1 *e*) or reduced (Fig. S3 *f*).

Finally, we would like to remind the reader about the potential limitations of this study and how they were addressed. At first, IRM as a technique has been extensively used in model membranes and RBCs but less so in adherent cells for membrane height measurement. To get proper measurements, we have performed checks (Fig. S9) to show that

in FBRs, local actin density (marked fluorescently) doesn't strongly alter reflectivity as also evident in studies using IRM showing actin localizing but affecting an IRM image only by pushing the membrane later (33). Similarly, in regions chosen for analysis (FBRs), we do not find a nonrandom correlation of movement of internal membranous structure (marked fluorescently) with IRM intensity fluctuations (Fig. S10). Any correlation found in both cases were still present on choosing random noncorresponding sets. The other important part of the study is the fitting of PSDs to a known model for extracting mechanical parameters. We emphasize that any trend in mechanical parameters reported herein was rigorously checked in multiple ways (Supporting Discussion) and observed even on changing the number (4–6) of fitting parameters. Furthermore, to verify if enhanced spatial heterogeneity in mechanical parameters is also visually distinguishable, we calculate values for each pixel and present the maps (Figs. 4 *e* and S4). Maps beautifully depict a uniform, although noisy, state of membrane tension in control cells. Pockets emerge in MβCD-treated cells in line with the intracellular heterogeneity evaluated by using averaged PSDs. Although the fitting is not perfect for each pixel as evident from the map of R^2 and mapping was extended beyond FBR pixels, these maps capture the central essence of this article and provide further support of the use of four-parameter fits. Interestingly, the factor "A" (implying active temperature) has a similar pattern as that of a Gaussian-ness map.

In conclusion, we show that under cholesterol depletion by MβCD, cells have altered fluctuations (enhanced flattening of spatial undulations and damping of temporal fluctuations) and show a clear increase in membrane tension. This work extends our understanding about the effect of MβCD on cells by demonstrating that it creates long-range heterogeneity or intracellular variability in membrane tension and enhances rupture rates and rupture diameter.

SUPPORTING MATERIAL

Supporting Material can be found online at https://doi.org/10.1016/j.bpj.2019.03.016.

AUTHOR CONTRIBUTIONS

Conceptualization, B.S.; Methodology, B.S., A.B., T.S., S.D., and P.K.; Software, B.S. and A.B.; Validation, A.B. and B.S.; Investigation, A.B., P.K., S.D., and T.S.; Formal Analysis, A.B. and P.K.; Data Curation: A.B.; Writing—Original Draft, B.S. and A.B.; Writing—Review & Editing, T.S. and P.K.; Visualization, A.B.; Supervision, B.S.; and Funding Acquisition, B.S.

ACKNOWLEDGMENTS

The authors are grateful to Indian Institute of Science Education and Research Kolkata for providing a scholarship to A.B., Department of Science and Technology-Innovation in Science Pursuit for Inspired Research for providing a scholarship to P.K., and to Kishore Vaigyanik Protsahan Yojana for providing fellowships to S.D. and T.S. We thank Rajesh Kumble Nayak for helping with the code to calculate PSD, Jayasri Das Sarma for HeLa cells, Rupak Datta for CHO cells, and Kaushik Sengupta (Saha Institute of Nuclear Physics, Kolkata) for the C2C12 cells.

This work was supported by the Wellcome Trust/Department of Biotechnology India Alliance Fellowship (grant IA/I/13/1/500885) awarded to B.S.

REFERENCES

1. Yeagle, P. L. 1985. Cholesterol and the cell membrane. *Biochim. Biophys. Acta.* 822:267–287.
2. Ikonen, E. 2008. Cellular cholesterol trafficking and compartmentalization. *Nat. Rev. Mol. Cell Biol.* 9:125–138.
3. Byfield, F. J., H. Aranda-Espinoza, …, I. Levitan. 2004. Cholesterol depletion increases membrane stiffness of aortic endothelial cells. *Biophys. J.* 87:3336–3343.
4. Goodwin, J. S., K. R. Drake, …, A. K. Kenworthy. 2005. Ras diffusion is sensitive to plasma membrane viscosity. *Biophys. J.* 89:1398–1410.
5. Shvartsman, D. E., O. Gutman, …, Y. I. Henis. 2006. Cyclodextrins but not compactin inhibit the lateral diffusion of membrane proteins independent of cholesterol. *Traffic.* 7:917–926.
6. Kwik, J., S. Boyle, …, M. Edidin. 2003. Membrane cholesterol, lateral mobility, and the phosphatidylinositol 4,5-bisphosphate-dependent organization of cell actin. *Proc. Natl. Acad. Sci. USA.* 100:13964–13969.
7. Sun, M., N. Northup, …, G. Forgacs. 2007. The effect of cellular cholesterol on membrane-cytoskeleton adhesion. *J. Cell Sci.* 120:2223–2231.
8. Norman, L. L., R. J. Oetama, …, H. Aranda-Espinoza. 2010. Modification of cellular cholesterol content affects traction force, adhesion and cell spreading. *Cell. Mol. Bioeng.* 3:151–162.
9. Dulhunty, A. F., and C. Franzini-Armstrong. 1975. The relative contributions of the folds and caveolae to the surface membrane of frog skeletal muscle fibres at different sarcomere lengths. *J. Physiol.* 250:513–539.
10. Parpal, S., M. Karlsson, …, P. Strålfors. 2001. Cholesterol depletion disrupts caveolae and insulin receptor signaling for metabolic control via insulin receptor substrate-1, but not for mitogen-activated protein kinase control. *J. Biol. Chem.* 276:9670–9678.
11. Richter, T., M. Floetenmeyer, …, R. G. Parton. 2008. High-resolution 3D quantitative analysis of caveolar ultrastructure and caveola-cytoskeleton interactions. *Traffic.* 9:893–909.
12. Fielding, C. J., and P. E. Fielding. 2000. Cholesterol and caveolae: structural and functional relationships. *Biochim. Biophys. Acta.* 1529:210–222.
13. Prescott, L., and M. W. Brightman. 1976. The sarcolemma of Aplysia smooth muscle in freeze-fracture preparations. *Tissue Cell.* 8:241–258.
14. Sinha, B., D. Köster, …, P. Nassoy. 2011. Cells respond to mechanical stress by rapid disassembly of caveolae. *Cell.* 144:402–413.
15. Irie, T., M. Otagiri, …, Y. Sugiyama. 1982. Cyclodextrin-induced hemolysis and shape changes of human erythrocytes in vitro. *J. Pharmacobiodyn.* 5:741–744.
16. Morris, C. E., and U. Homann. 2001. Cell surface area regulation and membrane tension. *J. Membr. Biol.* 179:79–102.
17. Kosmalska, A. J., L. Casares, …, P. Roca-Cusachs. 2015. Physical principles of membrane remodelling during cell mechanoadaptation. *Nat. Commun.* 6:7292.
18. Evans, E., and D. Needham. 1987. Physical properties of surfactant bilayer membranes: thermal transitions, elasticity, rigidity, cohesion and colloidal interactions. *J. Phys. Chem.* 91:4219–4228.

19. Needham, D., and R. S. Nunn. 1990. Elastic deformation and failure of lipid bilayer membranes containing cholesterol. *Biophys. J.* 58:997–1009.

20. Karatekin, E., O. Sandre, …, F. Brochard-Wyart. 2003. Cascades of transient pores in giant vesicles: line tension and transport. *Biophys. J.* 84:1734–1749.

21. Atger, V. M., M. de la Llera Moya, …, G. H. Rothblat. 1997. Cyclodextrins as catalysts for the removal of cholesterol from macrophage foam cells. *J. Clin. Invest.* 99:773–780.

22. Zidovetzki, R., and I. Levitan. 2007. Use of cyclodextrins to manipulate plasma membrane cholesterol content: evidence, misconceptions and control strategies. *Biochim. Biophys. Acta.* 1768:1311–1324.

23. Gidwani, B., and A. Vyas. 2015. A comprehensive Review on cyclodextrin-based carriers for delivery of chemotherapeutic cytotoxic anticancer drugs. *BioMed Res. Int.* 2015:198268.

24. Kowalsky, G. B., F. J. Byfield, and I. Levitan. 2008. oxLDL facilitates flow-induced realignment of aortic endothelial cells. *Am. J. Physiol. Cell Physiol.* 295:C332–C340.

25. Khatibzadeh, N., S. Gupta, …, B. Anvari. 2012. Effects of cholesterol on nano-mechanical properties of the living cell plasma membrane. *Soft Matter.* 8:8350–8360.

26. Levitan, I., T. P. Shentu, …, G. Forgacs. 2014. The role of cholesterol and lipoproteins in control of endothelial biomechanics. *In* Mechanobiology of the Endothelium. H. Aranda-Espinoza, ed. Taylor & Francis, pp. 146–165.

27. Alert, R., J. Casademunt, …, P. Sens. 2015. Model for probing membrane-cortex adhesion by micropipette aspiration and fluctuation spectroscopy. *Biophys. J.* 108:1878–1886.

28. Kaizuka, Y., and J. T. Groves. 2006. Hydrodynamic damping of membrane thermal fluctuations near surfaces imaged by fluorescence interference microscopy. *Phys. Rev. Lett.* 96:118101.

29. Rodríguez-García, R., I. López-Montero, …, F. Monroy. 2015. Direct cytoskeleton forces cause membrane softening in red blood cells. *Biophys. J.* 108:2794–2806.

30. Gárate, F., M. Pertusa, …, R. Bernal. 2018. Non-invasive neurite mechanics in differentiated PC12 cells. *Front. Cell. Neurosci.* 12:194.

31. Farago, O. 2011. Mechanical surface tension governs membrane thermal fluctuations. *Phys. Rev. E Stat. Nonlin. Soft Matter Phys.* 84:051914.

32. Curtis, A. S. 1964. The mechanism of adhesion of cells to glass. A study by interference reflection microscopy. *J. Cell Biol.* 20:199–215.

33. Case, L. B., and C. M. Waterman. 2011. Adhesive F-actin waves: a novel integrin-mediated adhesion complex coupled to ventral actin polymerization. *PLoS One.* 6:e26631.

34. Abercrombie, M., and G. A. Dunn. 1975. Adhesions of fibroblasts to substratum during contact inhibition observed by interference reflection microscopy. *Exp. Cell Res.* 92:57–62.

35. Rädler, J. O., and E. Sackmann. 1993. Imaging optical thicknesses and separation distances of phospholipid vesicles at solid surfaces. *J. Phys. II.* 3:727–748.

36. Godwin, S. L., M. Fletcher, and R. P. Burchard. 1989. Interference reflection microscopic study of sites of association between gliding bacteria and glass substrata. *J. Bacteriol.* 171:4589–4594.

37. Limozin, L., and K. Sengupta. 2009. Quantitative reflection interference contrast microscopy (RICM) in soft matter and cell adhesion. *ChemPhysChem.* 10:2752–2768.

38. Biswas, A., A. Alex, and B. Sinha. 2017. Mapping cell membrane fluctuations reveals their active regulation and transient heterogeneities. *Biophys. J.* 113:1768–1781.

39. Portet, T., and R. Dimova. 2010. A new method for measuring edge tensions and stability of lipid bilayers: effect of membrane composition. *Biophys. J.* 99:3264–3273.

40. Moroz, J. D., and P. Nelson. 1997. Dynamically stabilized pores in bilayer membranes. *Biophys. J.* 72:2211–2216.

41. McNeil, P. L., and R. A. Steinhardt. 1997. Loss, restoration, and maintenance of plasma membrane integrity. *J. Cell Biol.* 137:1–4.

42. Zhelev, D. V., and D. Needham. 1993. Tension-stabilized pores in giant vesicles: determination of pore size and pore line tension. *Biochim. Biophys. Acta.* 1147:89–104.

43. Thorpe, W. P., M. Toner, …, M. L. Yarmush. 1995. Dynamics of photo-induced cell plasma membrane injury. *Biophys. J.* 68:2198–2206.

44. Taupin, C., M. Dvolaitzky, and C. Sauterey. 1975. Osmotic pressure induced pores in phospholipid vesicles. *Biochemistry.* 14:4771–4775.

45. Klem, S., M. Klingler, …, B. Koletzko. 2012. Efficient and specific analysis of red blood cell glycerophospholipid fatty acid composition. *PLoS One.* 7:e33874.

46. Renard, H. F., M. Simunovic, …, L. Johannes. 2015. Endophilin-A2 functions in membrane scission in clathrin-independent endocytosis. *Nature.* 517:493–496.

47. Yahara, I., F. Harada, …, S. Natori. 1982. Correlation between effects of 24 different cytochalasins on cellular structures and cellular events and those on actin in vitro. *J. Cell Biol.* 92:69–78.

48. Helfrich, W. 1973. Elastic properties of lipid bilayers: theory and possible experiments. *Z. Naturforsch. C.* 28:693–703.

49. Simunovic, M., and G. A. Voth. 2015. Membrane tension controls the assembly of curvature-generating proteins. *Nat. Commun.* 6:7219.

50. Tenopoulou, M., T. Kurz, …, U. T. Brunk. 2007. Does the calcein-AM method assay the total cellular 'labile iron pool' or only a fraction of it? *Biochem. J.* 403:261–266.

51. Wilhelm, L. P., C. Wendling, …, F. Alpy. 2017. STARD3 mediates endoplasmic reticulum-to-endosome cholesterol transport at membrane contact sites. *EMBO J.* 36:1412–1433.

52. Gov, N., A. G. Zilman, and S. Safran. 2003. Cytoskeleton confinement and tension of red blood cell membranes. *Phys. Rev. Lett.* 90:228101.

53. Brochard, F., and J. F. Lennon. 1975. Frequency spectrum of the flicker phenomenon in erythrocytes. *J. Phys. (Paris).* 36:1035–1047.

54. Betz, T., and C. Sykes. 2012. Time resolved membrane fluctuation spectroscopy. *Soft Matter.* 8:5317–5326.

55. Lin, L. C., and F. L. Brown. 2004. Dynamics of pinned membranes with application to protein diffusion on the surface of red blood cells. *Biophys. J.* 86:764–780.

56. Peukes, J., and T. Betz. 2014. Direct measurement of the cortical tension during the growth of membrane blebs. *Biophys. J.* 107:1810–1820.

57. Gov, N., and S. A. Safran. 2005. Red blood cell shape and fluctuations: cytoskeleton confinement and ATP activity. *J. Biol. Phys.* 31:453–464.

58. Betz, T., M. Lenz, …, C. Sykes. 2009. ATP-dependent mechanics of red blood cells. *Proc. Natl. Acad. Sci. USA.* 106:15320–15325.

59. Thoumine, O., O. Cardoso, and J.-J. Meister. 1999. Changes in the mechanical properties of fibroblasts during spreading: a micromanipulation study. *Eur. Biophys. J.* 28:222–234.

60. Kim, T., M. L. Gardel, and E. Munro. 2014. Determinants of fluidlike behavior and effective viscosity in cross-linked actin networks. *Biophys. J.* 106:526–534.

61. Lieber, A. D., S. Yehudai-Resheff, …, K. Keren. 2013. Membrane tension in rapidly moving cells is determined by cytoskeletal forces. *Curr. Biol.* 23:1409–1417.

62. Campillo, C., P. Sens, …, C. Sykes. 2013. Unexpected membrane dynamics unveiled by membrane nanotube extrusion. *Biophys. J.* 104:1248–1256.

63. Simunovic, M., J. B. Manneville, …, A. Callan-Jones. 2017. Friction mediates scission of tubular membranes scaffolded by BAR proteins. *Cell.* 170:172–184.e11.

64. Gov, N., A. G. Zilman, and S. Safran. 2004. Hydrodynamics of confined membranes. *Phys. Rev. E Stat. Nonlin. Soft Matter Phys.* 70:011104.

65. Hochmuth, F. M., J. Y. Shao, …, M. P. Sheetz. 1996. Deformation and flow of membrane into tethers extracted from neuronal growth cones. *Biophys. J.* 70:358–369.

66. Monzel, C., D. Schmidt, …, R. Merkel. 2015. Measuring fast stochastic displacements of bio-membranes with dynamic optical displacement spectroscopy. *Nat. Commun.* 6:8162.

67. Battle, C., C. P. Broedersz, …, F. C. MacKintosh. 2016. Broken detailed balance at mesoscopic scales in active biological systems. *Science.* 352:604–607.

68. Thottacherry, J. J., A. J. Kosmalska, …, S. Mayor. 2018. Mechanochemical feedback control of dynamin independent endocytosis modulates membrane tension in adherent cells. *Nat. Commun.* 9:4217.

Biophysical Journal, Volume *116*

Supplemental Information

Cholesterol Depletion by MβCD Enhances Cell Membrane Tension and Its Variations-Reducing Integrity

Arikta Biswas, Purba Kashyap, Sanchari Datta, Titas Sengupta, and Bidisha Sinha

Table S1

Calculation of spatio-temporal parameters of membrane fluctuations			
Parameters	**Description**	**Types of averaging**	**Used in figures**
Mean relative height	Relative height of the membrane in a single pixel, calculated over 2048 frames	Averaged over 144 pixels to give one number per FBR	Figs. S1c, S3c, S5d
		Averaged over all FBRs to give one number per cell	Figs. S1b, S3b, S5c
SD_{time}	RMS value of temporal fluctuations in a single pixel, calculated over 2048 frames	Averaged over 144 pixels to give one number per FBR	Figs. S1c, S3c, S5d
		Averaged over all FBRs to give one number per cell	Figs. S1b, 3d, S5c
$SD(SD_{time})$	Intra-FBR variation of single-pixel RMS of temporal fluctuations, calculated over 2048 frames	Computed from 144 pixels to give one number per FBR	Figs. S1c, S6a
		Averaged over all FBRs to give one number per cell	Figs. 4a, S6a
SD SD_{time}	Intracellular heterogeneity in SD_{time}	SD calculated after clubbing SD_{time} values of all FBRs in a cell to give one number per cell	Fig. 4d
Dissimilar pairs	Intracellular variation of single-pixel RMS of temporal fluctuations	Computed from all FBRs to give one number per cell	Figs. 4b, S6b
SD_{space}	RMS value of spatial height variation in a 2.16x2.16 μm^2 region	Averaged in 20 frames to give one number per FBR	Figs. 2c, S3d, S5d
		Averaged over all FBRs to give one number per cell	Figs. 2d, S3d, S5c
SD SD_{space}	Intracellular heterogeneity in SD_{space}	SD calculated after clubbing SD_{space} values of all FBRs in a cell to give one number per cell	Fig. 4d
λ	Correlation length obtained in a 6.3x1.8 μm^2 region from fitting spatial ACFs to 3-term exponential function	Averaged over 200 frames to give one number per region	Figs. 2c, S5d
		Averaged over all regions to give one number per cell	Figs. 2d, S5c
τ	Correlation time obtained in a pixel by fitting	Averaged in a 0.36x0.36 μm^2 region to give one number per region	Fig. 3a

	temporal ACFs to 3-term exponential function	Averaged in a 2.16x2.16 μm^2 region to give one number per region	Fig. 3a inset
PSD	Power spectrum of temporal fluctuations	Averaged over 144 pixels to get one PSD per FBR	Figs. 2a, S3a, S5b
Parameters extracted from PSD			
Parameters	**Description**	**Types of averaging**	**Used in figures**
$\overline{\sigma(f_1, f_2)}$	Amplitude of temporal fluctuations in a frequency regime	Computed from a PSD to get one number per FBR	Figs. S1c, S3c, S5d
		Averaged over all FBRs to get one number per cell	Figs. 2a, S3b, S5c
Exponent	Frequency dependent power law of the PSD	Computed from a PSD to get one number per FBR	Figs. S1c, S3c, S5d
		Averaged over all FBRs to get one number per cell	Figs. 2a, S3b, S5c
Parameters extracted by fitting PSD			
Parameters	**Description**	**Types of averaging**	**Used in figures**
A	Active temperature	Computed from a PSD to get one number per FBR	Figs. S1e, S3f, S6d
		Averaged over all FBRs to get one number per cell	Figs. 2e, S3e, S6c
η_{eff}	Effective cytoplasmic viscosity	Computed from a PSD to get one number per FBR	Figs. S1e, S3f, S6d
		Averaged over all FBRs to get one number per cell	Figs. 2e, S3f, S6c
γ	Confinement of the membrane	Computed from a PSD to get one number per FBR	Figs. S1e, S3f, S6d
		Averaged over all FBRs to get one number per cell	Figs. 2e, S3e, S6c
σ	Membrane tension	Computed from a PSD to get one number per FBR	Figs. S1e, 3d, S6d
		Averaged over all FBRs to get one number per cell	Figs. 2e, 3d, S6c

Table S1: Calculation of spatio-temporal parameters of fluctuations and mechanical parameters.

Table S2

Parameters	Notation	Values in reports	References	Values calculated in this study
Active temperature	A	3	(1)	3.6±1.1
Effective cytoplasmic viscosity	η_{eff}	2-4*10^4 Pa.s	(2–4)	4162±2010 Pa.s
Bending rigidity	κ	10-50 k_BT	(5–7)	Kept constant at 15 k_BT (8)
Confinement	γ	2.3*10^8 N/m3, 1.7*105 J/m4	(7, 9)	8.9±4.2x10^8 N/m^3
Membrane tension	σ	3.31*10^{-5} N/m, 10-100 pN/μm, 22-276 pN/μm	(6, 10–12)	565±330 pN/μm

Table S2: Description of the model which is used to extract mechanical parameters.

Figure S1

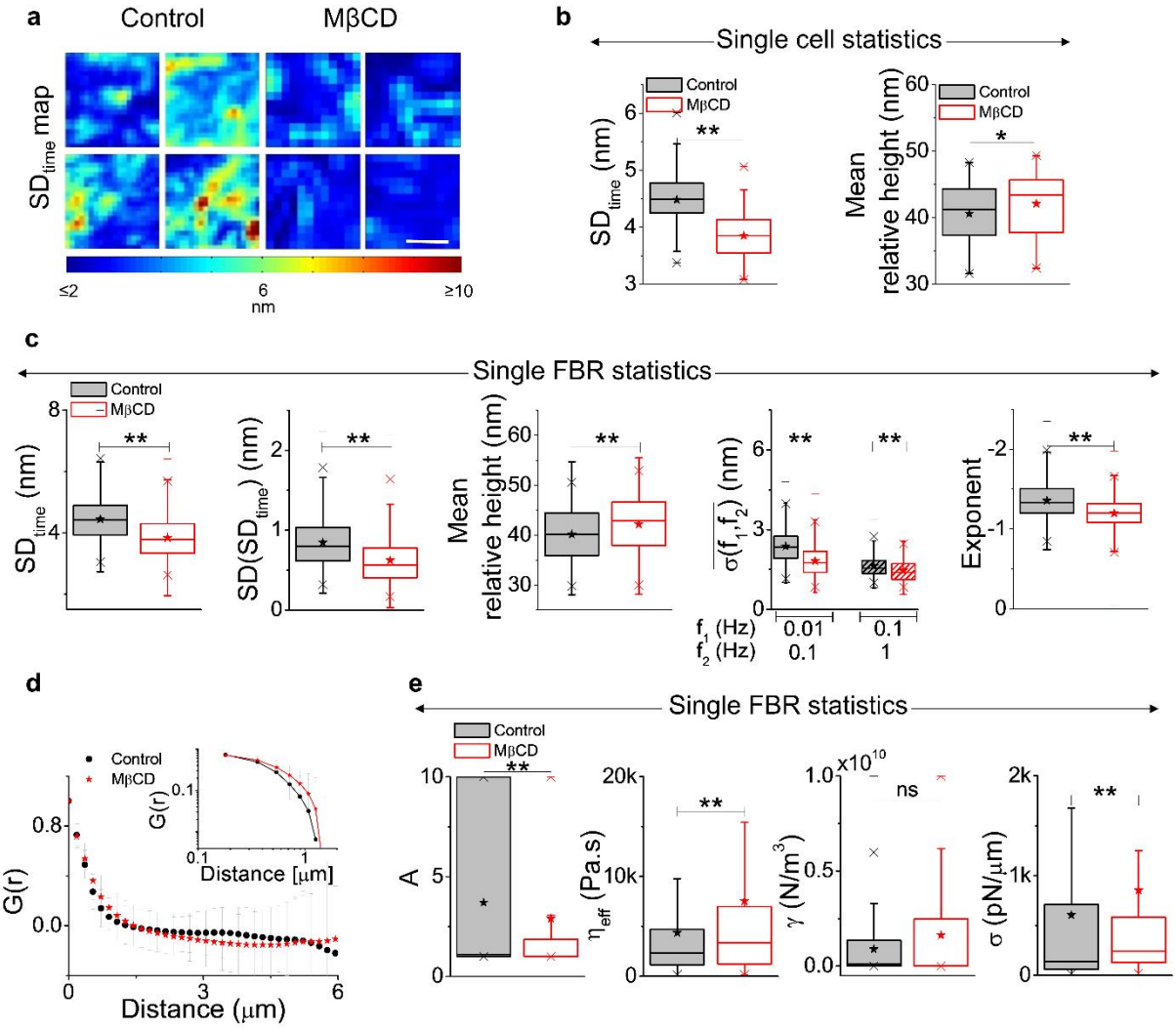

Figure S1: Effect of MβCD on detailed parameters of membrane fluctuations. (a) SD_{time} maps of representative FBRs in control and MβCD treated cells (scale bar: 1 μm). (b) Box plots of SD_{time} and mean relative height in the two conditions. N = 70 cells each. (c) Single FBR statistics of parameters of temporal fluctuations in the two conditions. $n_{control}$ = 1683 FBRs, $n_{M\beta CD}$ = 1471 FBRs, N = 70 cells each. (d) Averaged spatial ACFs (and their log-log plots, top inset) for control and cholesterol depleted cells. (e) Single FBR statistics of mechanical parameters in control vs. cholesterol depleted cells. $n_{control}$ = 1500 FBRs, $n_{M\beta CD}$ = 1317 FBRs, N = 70 cells each. * p value < 0.05, ** p value < 0.001, ns p value > 0.05, Mann-Whitney U test. See **Table S4** for statistics.

Figure S2

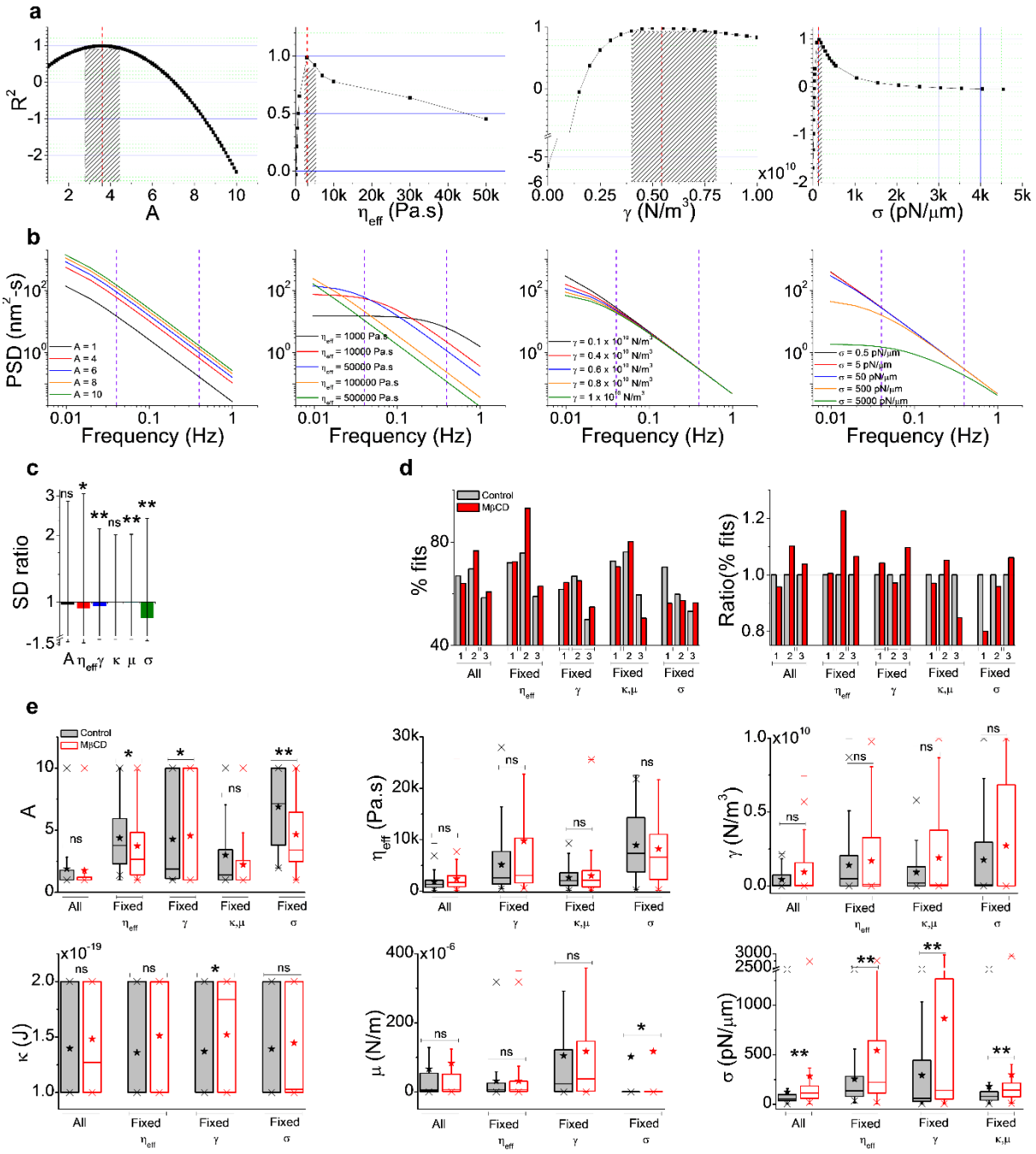

Figure S2: Alterations in membrane tension primarily rule the change in fluctuations. (a) Plots of calculated R^2 with different values of A, η_{eff}, γ, σ to check the sensitivity of the extracted mechanical parameters. (b) Simulations of PSD $PSD(f) = \frac{4\eta_{eff}Ak_BT}{\pi}\int_{q_{min}}^{q_{max}} \frac{dq}{(4\eta_{eff}(2\pi f))^2+\left[\kappa q^3+\sigma q+\frac{\gamma}{q}\right]^2}$ with changing values of A, η_{eff}, γ, σ from low to high numbers to check the robustness of the parameters. The basic power spectrum was constructed with these parameters: A = 1.8083, η_{eff} = 3838 Pa.s, γ = 0.16 x 1010 N/m3, κ = 0.6 x 10-19 J, σ = 74.8 pN/μm. The dashed vertical lines show the regime where the exponent is calculated. (c) Average values of SD ratio simulated from using one-ON approach in MβCD treated (left,

n = 616 simulations) cells of all six parameters. Error bars represent the standard deviation values in each. PSDs $PSD(f) = \frac{4\eta_{eff}Ak_BT}{\pi}\int_{q_{min}}^{q_{max}} \frac{dq}{(4\eta_{eff}(2\pi f))^2+\left[\kappa q^3+\frac{9k_BT}{16\pi\kappa}\mu q+\sigma q+\frac{\gamma}{q}\right]^2}$ are simulated from different sets of observed fitting parameters. A whole set of fitting parameters corresponding to a control set are chosen and then only one parameter is changed at a time to that of a MβCD treated set. This is done for each of the parameters – A to σ. The ratio of the SD of the original control set and the SD calculated from the simulated PSD is calculated and the log of these values are plotted to understand the different contributions. Statistics is by students' t-test. (d) Left: plot of % fits in all categories mentioned below in three sets of experiments under control and MβCD treated conditions. $\%\, fits = \frac{No.of\ FBRs\ that\ fit\ to\ the\ model\ in\ the\ mentioned\ category}{Total\ no.of\ FBRs\ analyzed}$. Right: plot of ratio (% fits) between control and MβCD treated cells in the same criteria across three sets of experiments. $Ratio\ (\%\, fits) = \frac{\%\, fits\ in\ M\beta CD\ sets}{\%\, fits\ in\ control\ treated\ sets}$. n = 10 cells each. (e) Mechanical parameters extracted from fitting the PSDs to the theoretical model with minor modifications of control and cholesterol depleted cells. All: none of the parameters are fixed, Fixed η_{eff}: η_{eff} = 3421.27 Pa.s, Fixed γ: γ = 0.08x10^{10} N/m^3, Fixed κ, μ: κ = 1.38x10^{-19} J & μ = 90x10^{-6} N/m, Fixed σ : σ = 368 pN/μm. N = 10 cells, $n_{control}$ = 188 total FBRs, $n_{M\beta CD}$ = 186 total FBRs. * p value < 0.05, ** p value < 0.001, Mann-Whitney U test. See **Table S4** for statistics.

Figure S3

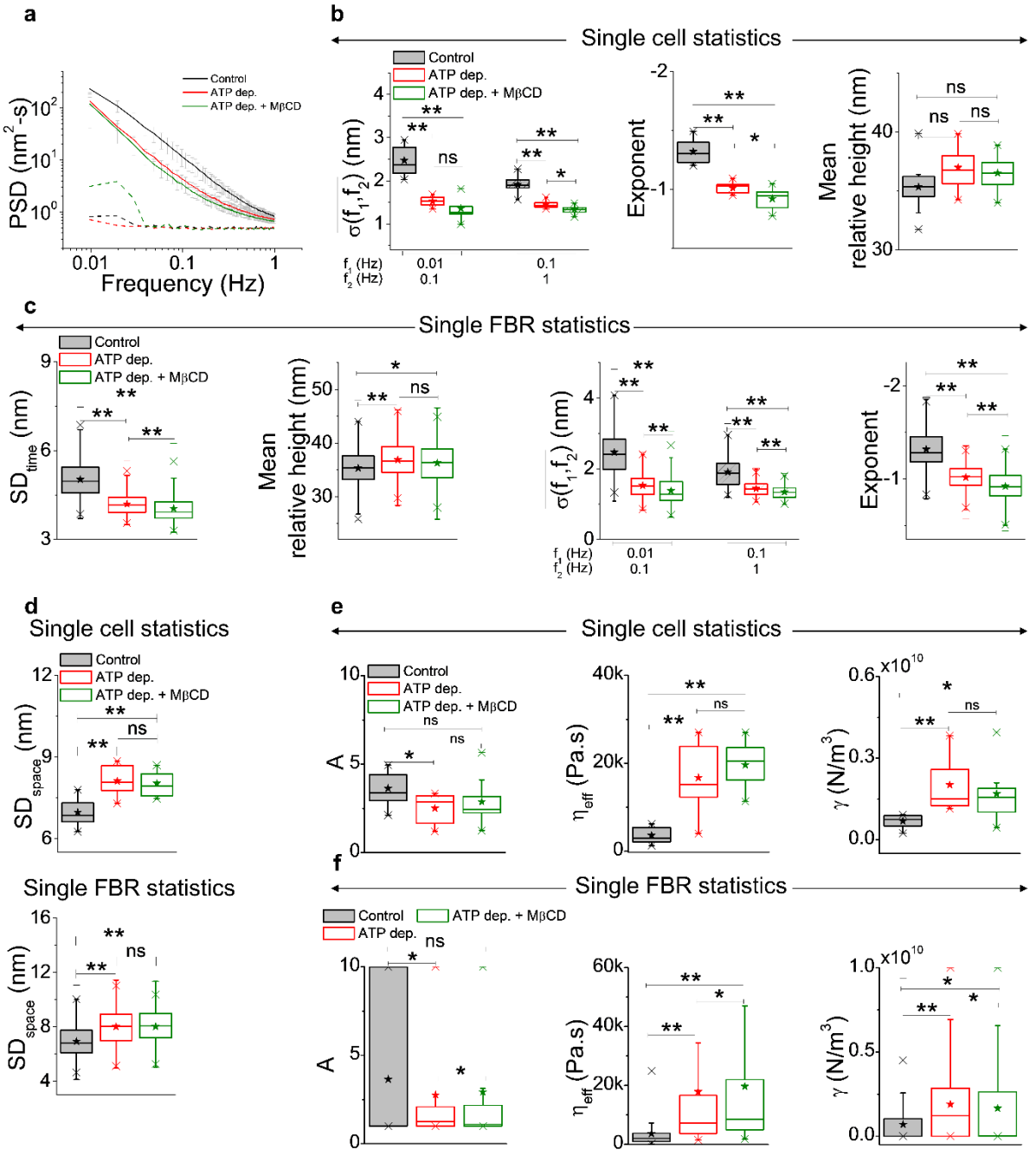

Figure S3: Effect of MβCD on ATP depleted cells. (a) Averaged PSDs of cells (solid lines) and their backgrounds (dashed lines) in control, ATP dep. and ATP dep. + MβCD cells. (b) Single cell statistics of parameters of temporal fluctuations in these conditions. N = 10 cells each. (c) Single FBR statistics of temporal fluctuations parameters in the three mentioned conditions. $n_{control}$ = 333 FBRs, $n_{ATPdep.}$ = 235 FBRs, $n_{ATPdep.+M\beta CD}$ = 250 FBRs, N = 10 cells each. (d) Single cell statistics (top, N = 10 cells each) and single FBR statistics (bottom, $n_{control}$ = 333 FBRs, $n_{ATPdep.}$ = 235 FBRs, $n_{ATPdep.+M\beta CD}$ = 229 FBRs, N = 10 cells each) of SD_{space} in all three conditions. (e) Box plots of A, η_{eff} and γ for single cell statistics. N = 10 each. (f) Single FBR statistics of the mechanical parameters in the three conditions. $n_{control}$ = 305 FBRs,

$n_{ATPdep.}$ = 207 FBRs, $n_{ATPdep.+M\beta CD}$ = 229 FBRs, N = 10 cells each. * p value < 0.05, ** p value < 0.001, ns p value > 0.05, Mann-Whitney U test. See **Table S4** for statistics.

Figure S4

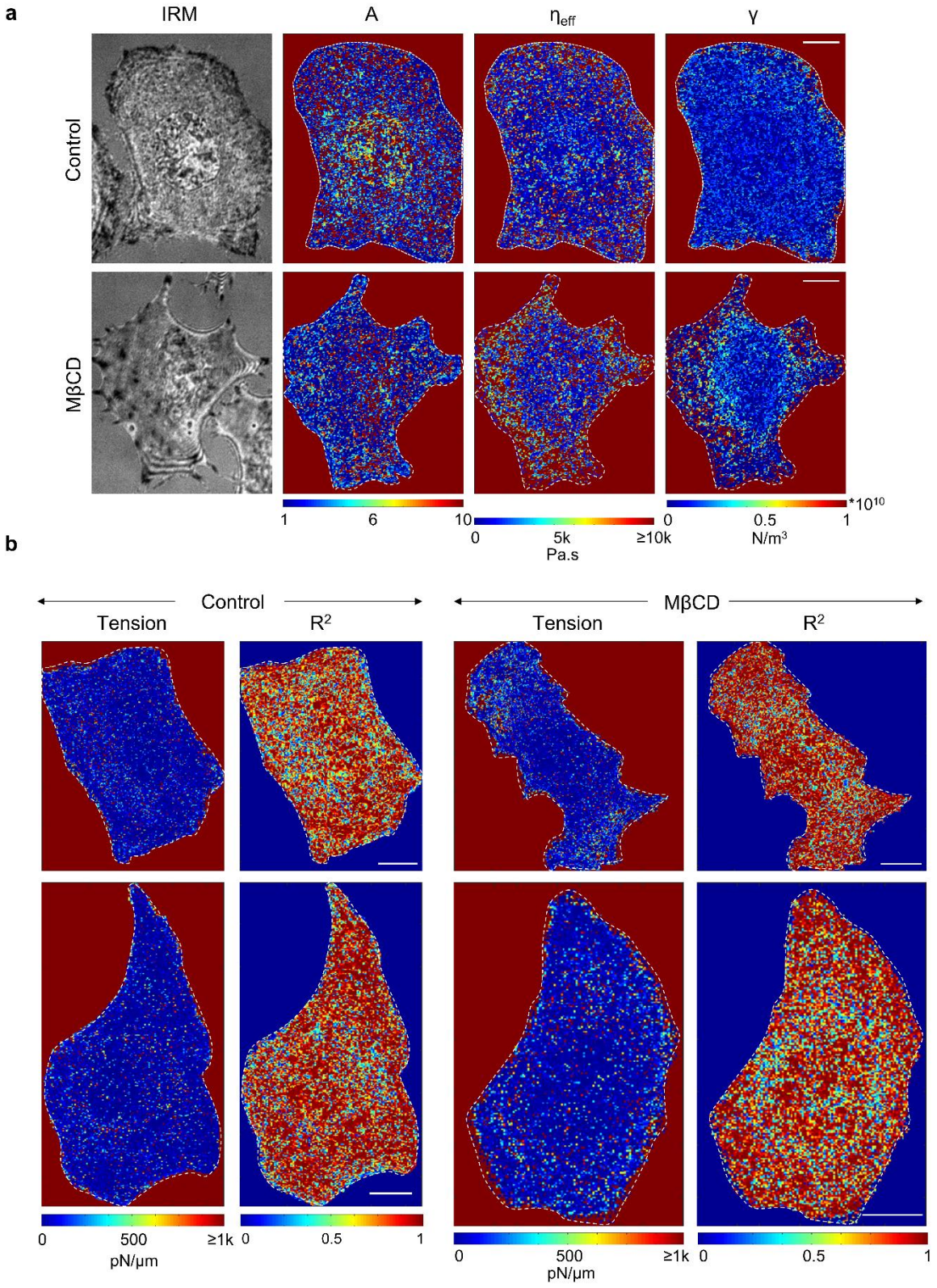

Figure S4: Maps of mechanical parameters on MβCD treatment. (a) Representative IRM images with single pixel maps of active temperature, cytoplasmic viscosity and confinement of a control and MβCD treated cell (tension map in Fig. 4e). Scale bar, 10 µm. The white dashed

lines mark the cell boundary. Fitting was performed for pixels inside this boundary. (b) Two representative single pixel maps of tension and R^2 for control and cholesterol depleted cells. Scale bar, 10 μm. The white dashed lines mark the cell boundary. Fitting was performed for pixels inside this boundary.

Figure S5

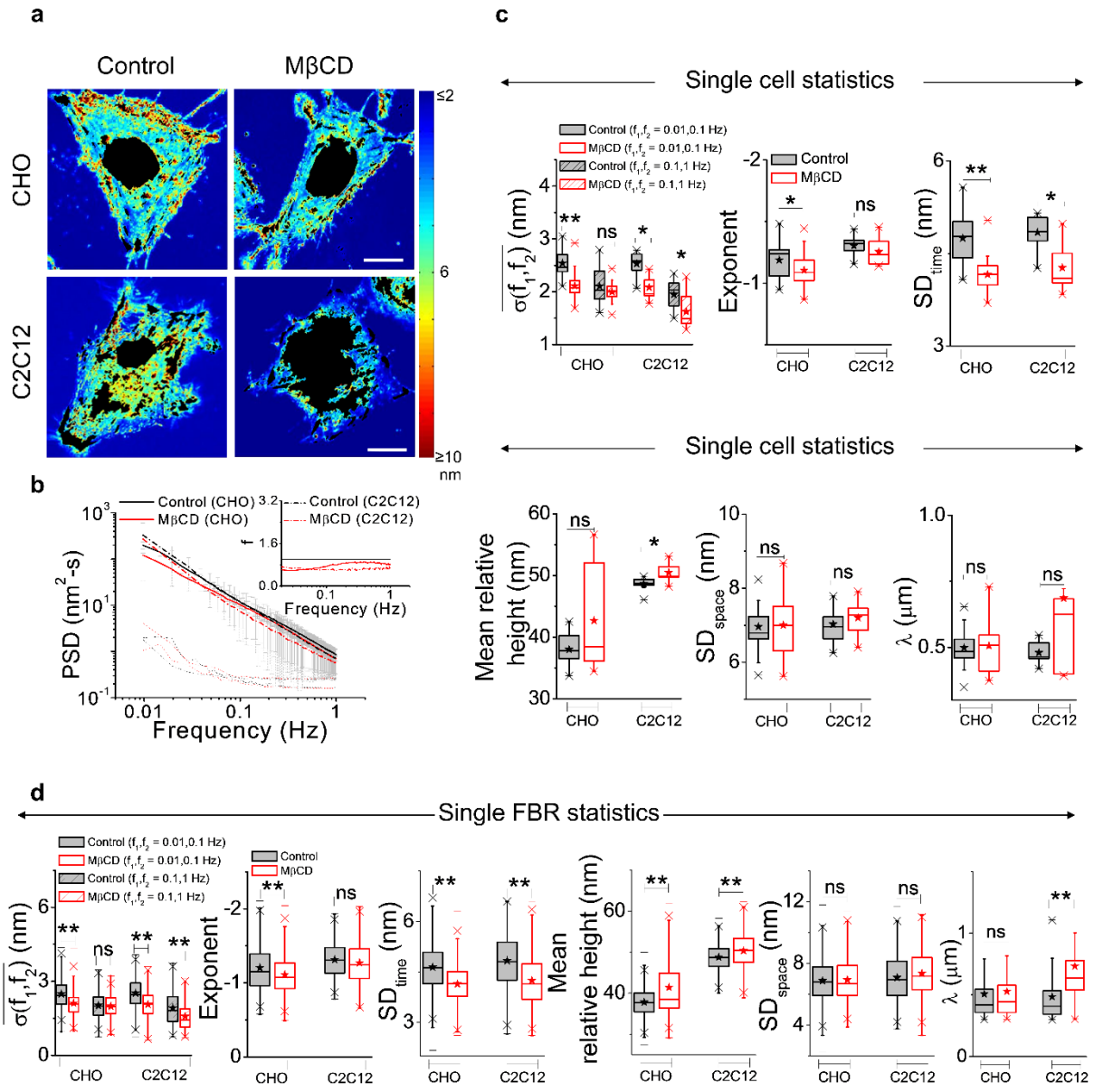

Figure S5: Effect of MβCD on detailed parameters of membrane fluctuations in different cell lines. (a) Representative whole cell SD_{time} maps of control vs. MβCD treated CHO (top, scale bar: 10 µm) and C2C12 (bottom, scale bar: 5 µm) cells. Non-FBRs are blackened out. (b) Averaged PSDs of CHO (solid lines) and C2C12 (dashed lines) cells in control and cholesterol depleted conditions with their respective backgrounds (dash and dotted lines); inset shows the ratio of the background subtracted PSDs of the two cell lines. (c) Box plots of single cell statistics for the parameters of temporal fluctuations and spatial undulations in both conditions for the two cell lines. N = 30 cells each in CHO, 10 cell each in C2C12. (d) Box plots of single FBR statistics for the parameters of temporal fluctuations and spatial undulations in both conditions for the two cell lines. $n_{CHO\ control}$ = 612 FBRs, $n_{CHO\ M\beta CD}$ = 369 FBRs, N = 30 cells each; $n_{C2C12\ control}$ = 219 FBRs, $n_{C2C12\ M\beta CD}$ = 179 FBRs, N = 10 cells each). * p value < 0.05, ** p value < 0.001, ns p value > 0.05, Mann-Whitney U test. See **Table S4** for statistics.

Figure S6

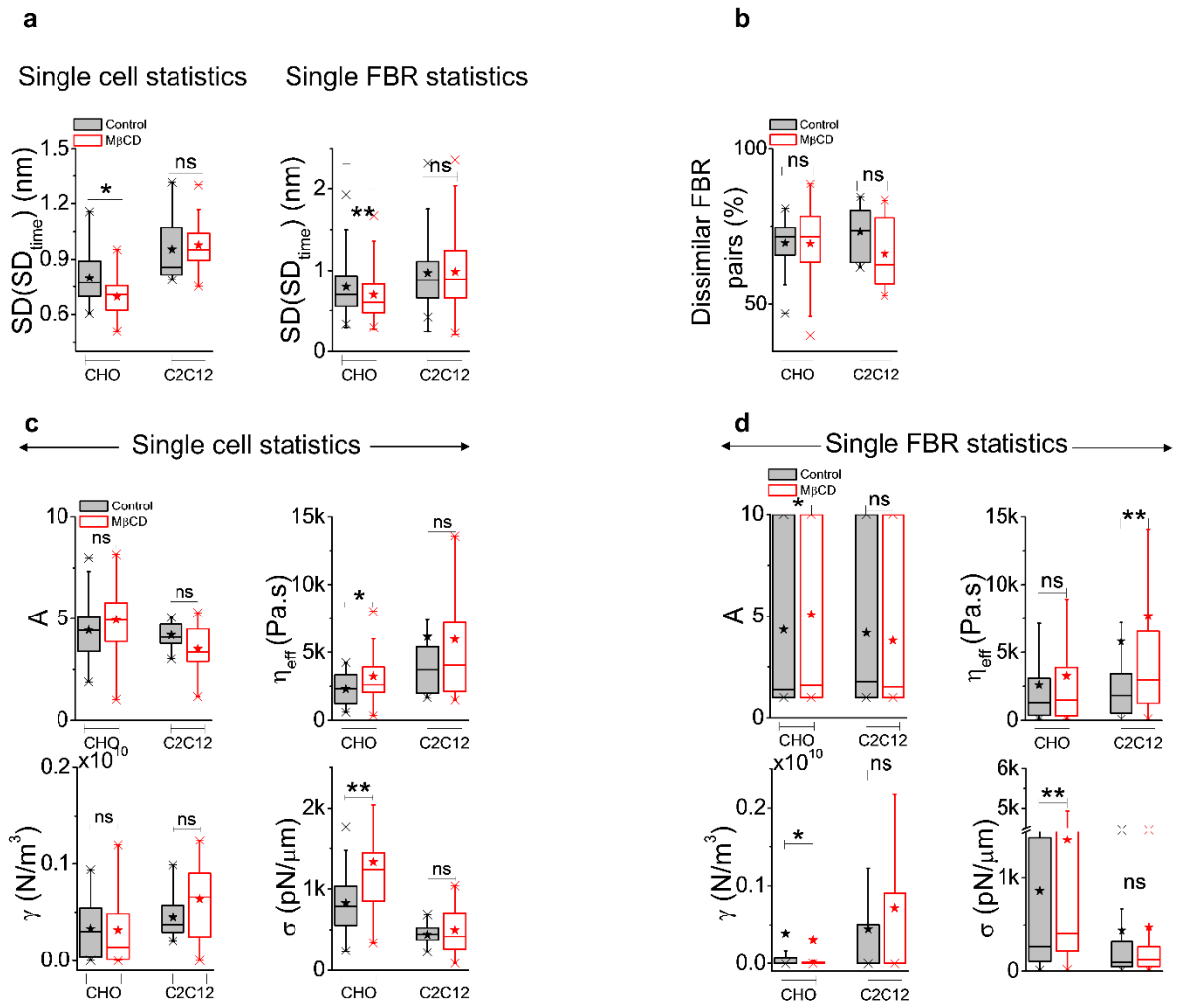

Figure S6: Effect of MβCD on fluctuations heterogeneity and mechanics in different cell lines. (a) A measure of intra-FBR fluctuations heterogeneity, $SD(SD_{time})$ in control and MβCD treated CHO and C2C12 cells in single cell statistics (left, N = 30 cell each for CHO, 10 cells each for C2C12) and single FBR statistics (right, $n_{CHO\ control}$ = 612 FBRs, $n_{CHO\ M\beta CD}$ = 369 FBRs, N = 30 cells each; $n_{C2C12\ control}$ = 219 FBRs, $n_{C2C12\ M\beta CD}$ = 179 FBRs, N = 10 cells each). (b) Intracellular long-range heterogeneity (dissimilar FBR pairs) in CHO (N = 30 cells each) and C2C12 cells (N = 10 cells each). (c) Membrane mechanical parameters A, η_{eff}, γ and σ obtained from fitting PSDs in CHO (N = 30 cells each) and C2C12 cells (N = 10 cells each) in control and cholesterol depletion. (d) Single FBR statistics of the mechanical parameters under the two conditions in the two cell lines. $n_{CHO\ control}$ = 495 FBRs, $n_{CHO\ M\beta CD}$ = 257 FBRs, N = 30 cells each; $n_{C2C12\ control}$ = 174 FBRs, $n_{C2C12\ M\beta CD}$ = 124 FBRs, N = 10 cells each. * p value < 0.05, ** p value < 0.001, ns p value > 0.05, Mann-Whitney U test. See **Table S4** for statistics.

Figure S7

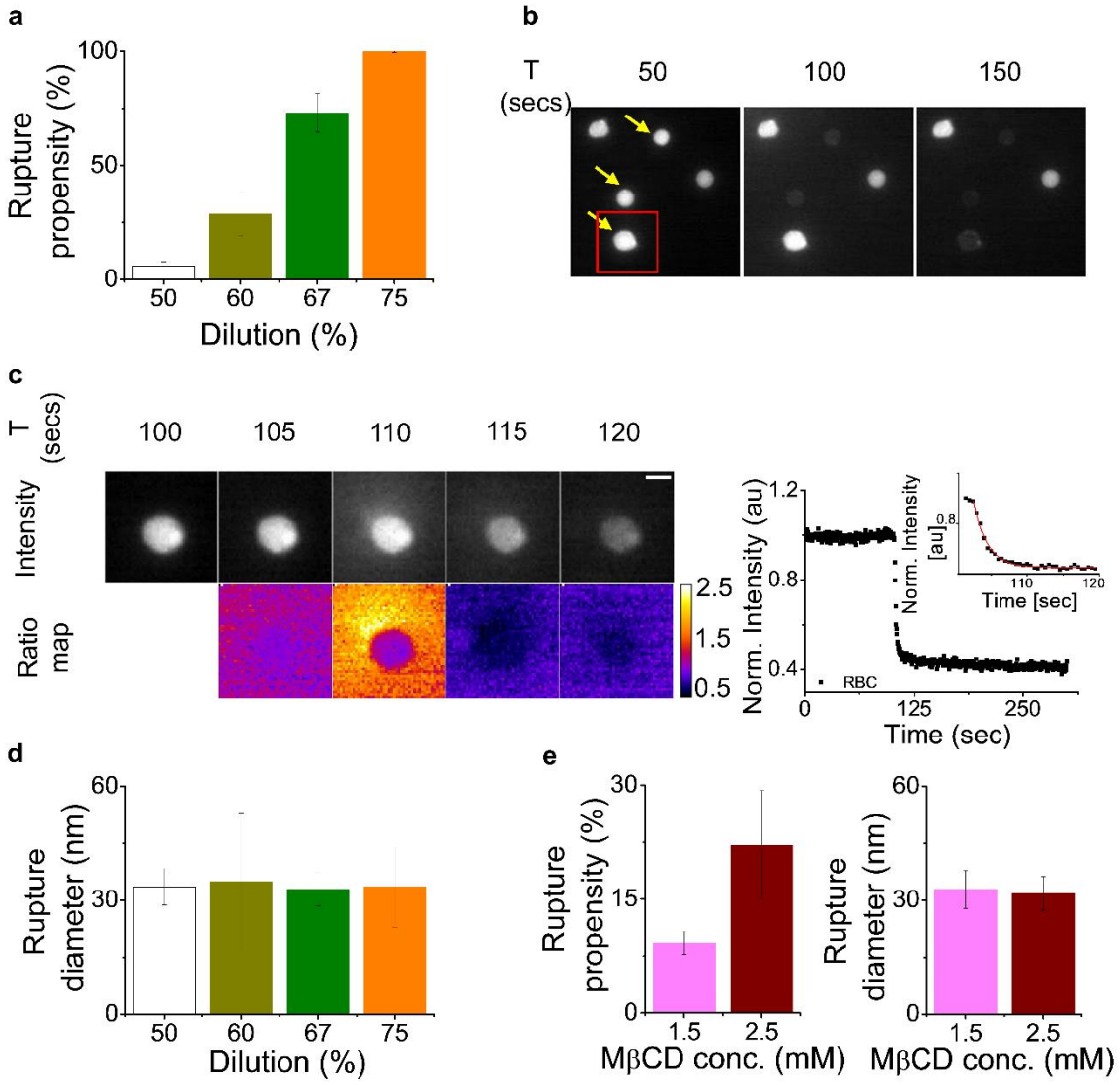

Figure S7: Rupture characteristics of RBCs. (a) Rupture propensity of RBCs with increase in osmotic stress. (b) Time lapse images of Calcein AM loaded RBCs undergoing rupture (arrows in yellow). (c) Intensity (top) and ratio map (bottom) of a rupturing RBC marked in (b) followed in time shows single point rupture. Right: A time profile of normalized mean intensity of a ruptured RBC; inset shows the double exponential fit to the profile. (d) Rupture diameter in RBCs with change in osmotic stress. (e) Rupture propensity (left) and rupture diameter (right) of RBCs treated with increasing concentrations of MβCD without hypo-osmotic shock administration. Mean ± SD of at least two experiments is plotted in each set. See **Table S4** for statistics.

Figure S8

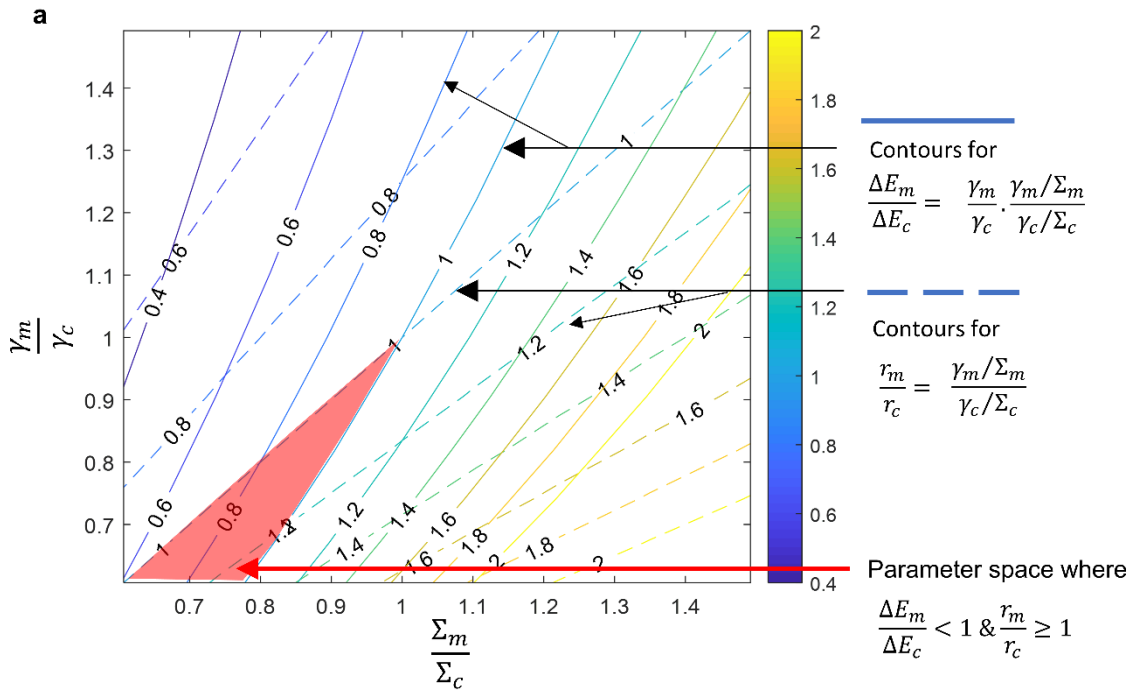

Figure S8: Lowered lysis surface and line tension on MβCD treatment. Contour plots of dependence of ratio of rupture radius of MβCD with control ($\frac{r_m}{r_c}$) & ratio of ΔE of MβCD with control ($\frac{\Delta E_m}{\Delta E_c}$) on the ratio of lysis surface tension between MβCD and control conditions ($\frac{\Sigma_m}{\Sigma_c}$) and on ratio of line tension between MβCD and control conditions ($\frac{\gamma_m}{\gamma_c}$). Contour lines closest to 1 are used to roughly map out the region in the parameter space where the observation of increased rupture propensity of ΔE ratio <1 and unchanged or increased rupture size ratio r ≥ 1 is true. Note that in this region both lysis surface tension ratio and line tension ratio (MβCD to control) is < 1, indicating lowered lysis surface and line tension on MβCD.

Figure S9

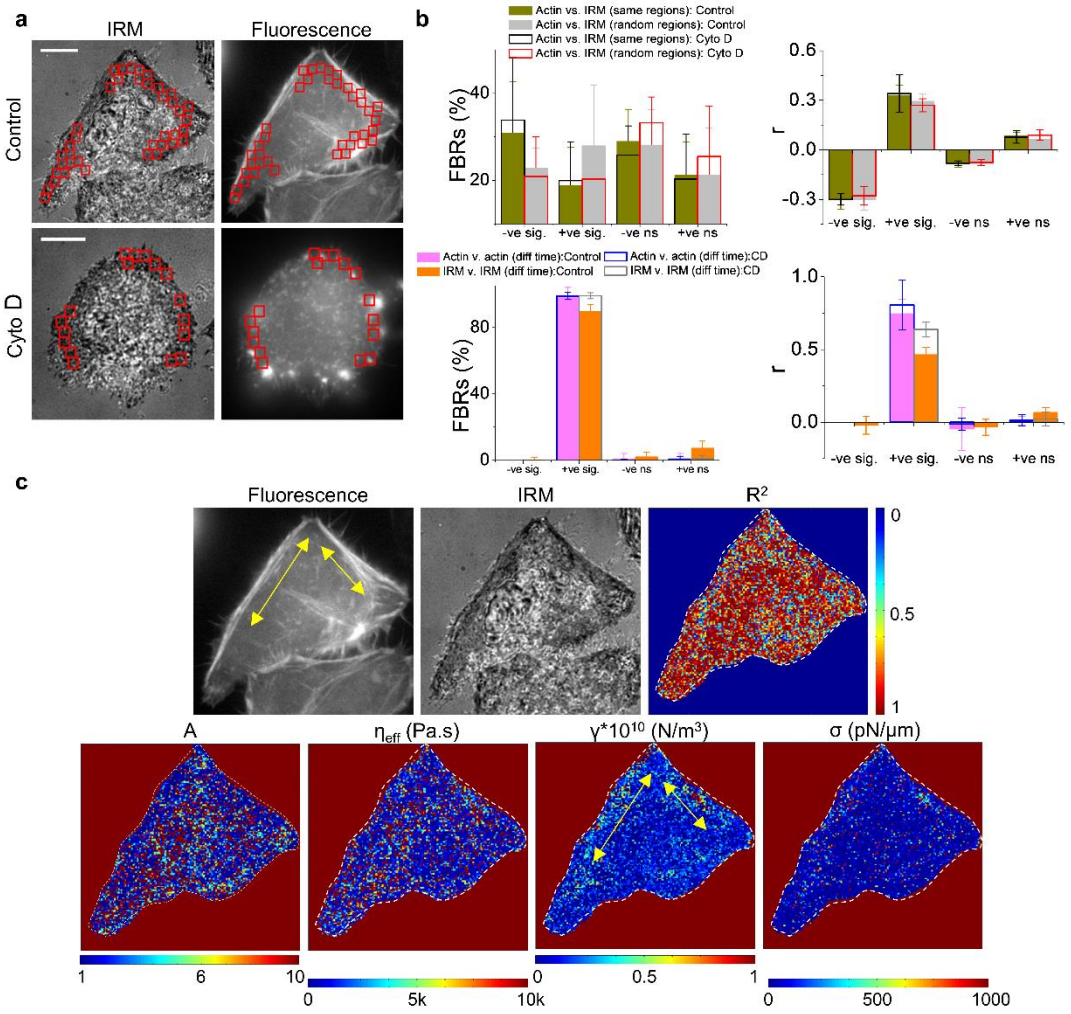

Figure S9: Actin density does not strongly affect IRM intensity at FBRs. (a) IRM and epi-fluorescence images of mEmerald-Lifeact-7 transfected control (top) and Cyto D treated (bottom) HeLa cells. Scale bar, 5 μm. (b) Top: plots of no of FBRs that show positive/negative correlation in actin and IRM intensities of same and random FBRs in control and Cyto D treated cells with their corresponding average Pearson correlation coefficients (r). Bottom: plots of no of FBRs that show positive/negative correlation in actin vs. actin and IRM vs. IRM intensities of same FBRs in and Cyto D treated cells with their corresponding average Pearson correlation coefficients (r). (c) Clockwise from top left: Fluorescence and IRM image of a control transfected cell, with its corresponding single pixel R^2, σ, γ, η_{eff} and A maps. The white dashed line marks the boundary of the cell. The yellow arrows mark the areas in confinement maps that faintly show the presence of stress fibres. Scale bar, 10 μm.

Figure S10

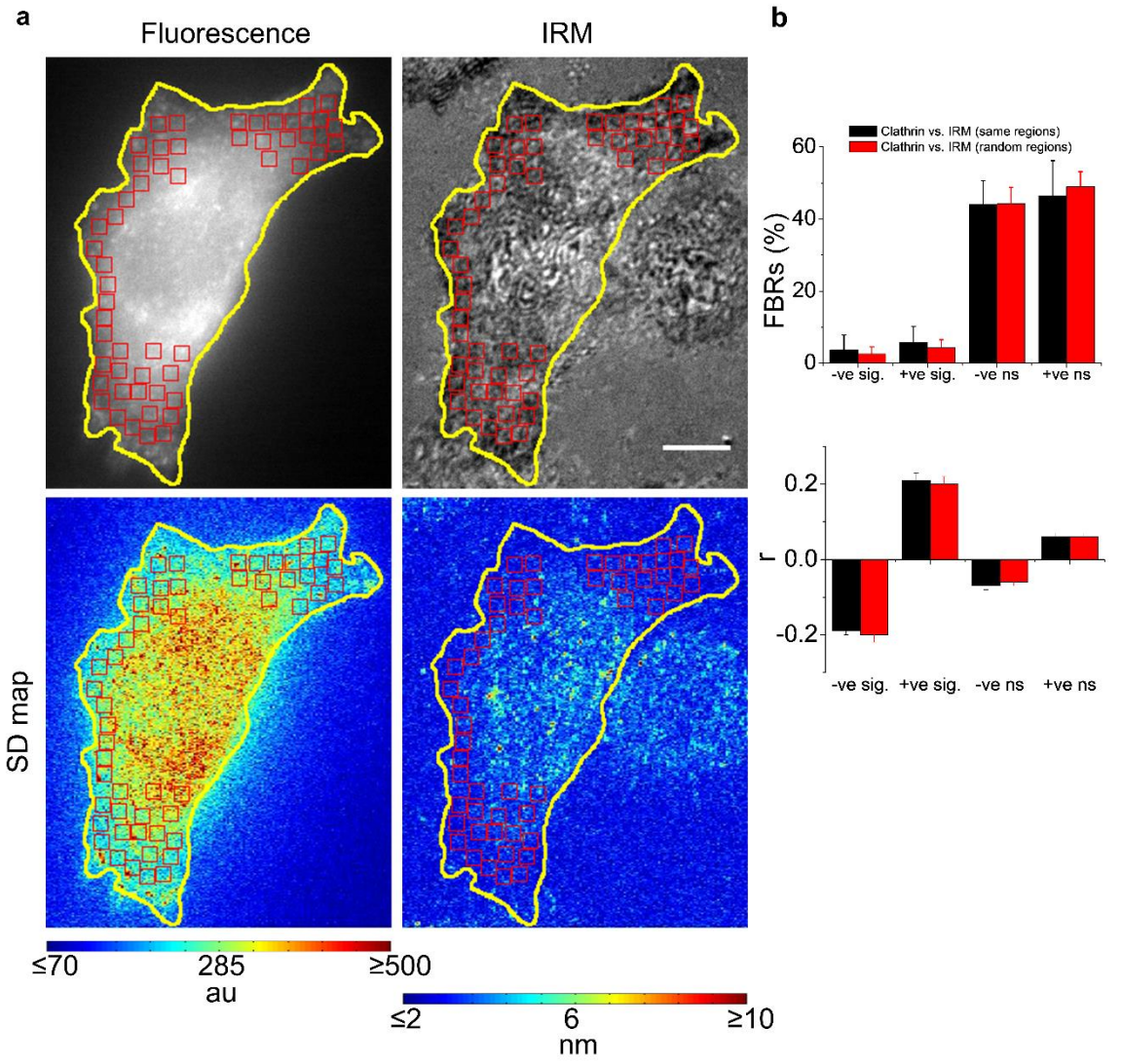

Figure S10: Mobile clathrin pits do not strongly affect IRM intensity fluctuations at FBRs. (a) Epi-fluorescence and IRM (top) images of mCherry-Clathrin LC-15 transfected control HeLa cells, with their corresponding SD maps (bottom). The boundary of the cell is marked in yellow. Scale bar, 10 μm. (b) Plots of no of FBRs that show positive/negative correlation in clathrin and IRM intensity fluctuations of same and random FBRs in cells (top) with their corresponding average Pearson correlation coefficients (r, bottom).

Supplementary Discussion

As elaborated in the reference (13), the energy needed to form a circular pore in the lipid bilayer can be written in terms of the line tension (γ), surface tension (Σ) and the radius of the pore (r):

$$E(r) = 2\pi r\gamma - \pi r^2\Sigma$$

The surface tension at the time of rupture can be termed as lysis tension.

Minimizing energy ($\frac{dE}{dr} = 0$), yields $r = \frac{\gamma}{\Sigma}$ (1)

The energy required to cross this critical radius r can be written as: $\Delta E = \frac{\pi\gamma^2}{\Sigma}$ (2)

In this study, we have two conditions where control is denoted as 'c' and MβCD treatment is denoted 'm'. From experiments, we see that MβCD treatment increases propensity (Fig. S6e). Since the propensity, or probability to rupture in isotonic conditions is expected to be related thus: $P \propto e^{\frac{-\Delta E}{k_B T}}$, this implies

$$\frac{\Delta E_m}{\Delta E_c} < 1 \quad \text{or,} \quad \frac{\gamma_m^2/\Sigma_m}{\gamma_c^2/\Sigma_c} < 1 \quad \text{or,} \quad \frac{\gamma_m}{\gamma_c}.\frac{\gamma_m/\Sigma_m}{\gamma_c/\Sigma_c} < 1 \tag{3}$$

But, we also know that rupture diameter is unaltered on MβCD treatment (Fig. S6d)

$$\frac{r_m}{r_c} = 1 \quad \text{or,} \quad \frac{\gamma_m/\Sigma_m}{\gamma_c/\Sigma_c} = 1 \tag{4}$$

From Eq. 3 and 4, it is evident that:

$$\frac{\gamma_m}{\gamma_c} < 1 \tag{5}$$

This information, together with Eq. 4 implies that $\frac{\Sigma_m}{\Sigma_c} < 1$

or, that the lysis tension of MβCD treated cells needs to be lower than that of control cells.

Observations of increased rupture diameter ($\frac{r_m}{r_c} > 1$) on MβCD treatment (Fig. 4 e) in hypo-tonic condition are in line with this inference since enhanced propensity would still need the line tension and hence lysis tension to be lowered by MβCD treatment.

Table S3: Statistical parameters for data presented in main figures.

This is provided as a separate Excel sheet

Table S4: Statistical parameters for data presented in supplementary figures.

This is provided as a separate Excel sheet

Supplementary Movies

Movie S1: Time-lapse imaging of single HeLa cells under control and MβCD treated conditions at 37 ºC under IRM mode.

The movie shows the time evolution of the interference pattern of the basal membrane of single HeLa cells in control (left) and MβCD treated (right) condition. Scale bar: 10 μm. Stacks of 2048 images are captured at 19.91 frames/sec.

Movie S2: Time-lapse imaging of control and MβCD treated HeLa cells after administration of 95% hypo-osmotic shock at 37 ºC.

The movie shows the time evolution of the fluorescence of Calcein AM loaded HeLa cells under control (left) and with MβCD (right), after the application of a 95% hypo-osmotic shock. Scale bar: 100 μm. Images are captured every 2 secs for 5 mins.

Movie S3: Time-lapse imaging of RBCs before and after administration of 67% hypo-osmotic shock at 37 ºC.

The movie shows the time evolution of the fluorescence of Calcein AM loaded RBCs before (left) and after (right) the application of a 67% hypo-osmotic shock. Scale bar: 100 μm. Images are captured every 0.5 secs for 5 mins.

Movie S4: Time-lapse imaging of MβCD treated RBCs without the administration of 67% hypo-osmotic shock at 37 ºC.

The movie shows the time evolution of the fluorescence of Calcein AM loaded RBCs that are treated with 1.5 mM (left) and 2.5 mM (right) MβCD without the application of a 67% hypo-osmotic shock. Scale bar: 100 μm. Images are captured every 0.5 secs for 5 mins.

Supplementary References

1. Gov, N., A.G. Zilman, and S. Safran. 2003. Cytoskeleton confinement and tension of red blood cell membranes. Phys. Rev. Lett. 90: 228101.

2. Thoumine, O., O. Cardoso, and J.-J. Meister. 1999. Changes in the mechanical properties of fibroblasts during spreading: a micromanipulation study. Eur Biophys J. 28: 222–234.

3. Kim, T., M.L. Gardel, and E. Munro. 2014. Determinants of Fluidlike Behavior and Effective Viscosity in Cross-Linked Actin Networks. Biophys. J. 106: 526–534.

4. Joanny, J., and J. Prost. 2009. Active gels as a description of the actin-myosin cytoskeleton. HFSR J. 3: 94–104.

5. Betz, T., M. Lenz, J.-F. Joanny, and C.C. Sykes. 2009. ATP-dependent mechanics of red blood cells. PNAS. 106: 15320–15325.

6. Peukes, J., and T. Betz. 2014. Direct Measurement of the Cortical Tension during the Growth of Membrane Blebs. Biophys. J. 107: 1810–1820.

7. Alert, R., J. Casademunt, J. Brugués, and P. Sens. 2015. Model for Probing Membrane-Cortex Adhesion by Micropipette Aspiration and Fluctuation Spectroscopy. Biophys. J. 108: 1878–1886.

8. Simunovic, M., and G.A. Voth. 2015. Membrane tension controls the assembly of curvature-generating proteins. Nat. Commun. 6: 1–8.

9. Curie, M., S. Bernard, and P. Cedex. 2008. 3D Processing and Analysis with ImageJ e. Microscopy. Vi: 1–6.

10. Sens, P., and J. Plastino. 2015. Membrane tension and cytoskeleton organization in cell motility. J. Phys. Condens. Matter. 27: 273103.

11. Lieber, A.D., S. Yehudai-Resheff, E.L. Barnhart, J.A. Theriot, and K. Keren. 2013. Membrane Tension in Rapidly Moving Cells Is Determined by Cytoskeletal Forces. Curr. Biol. 23: 1409–1417.

12. Betz, T., and C. Sykes. 2012. Time resolved membrane fluctuation spectroscopy. Soft Matter. 8: 5317.

13. Moroz, J.D., and P. Nelson. 1997. Dynamically Stabilized Pores in Bilayer Membranes. Biophys. J. 72: 2211–2216.